applied sciences

MDPI

Article

Aerodynamic Optimization and Analysis of Low Reynolds Number Propeller with Gurney Flap for Ultra-High-Altitude Unmanned Aerial Vehicle

Yuan Yao, Dongli Ma, Liang Zhang *, Xiaopeng Yang and Yayun Yu

School of Aeronautical Science and Engineering, Beihang University, Beijing 100191, China; fanfusuziyy@163.com (Y.Y.); madongli@buaa.edu.cn (D.M.); xiaopengyang@buaa.edu.cn (X.Y.); yuyayun@buaa.edu.cn (Y.Y.)

* Correspondence: microbeast@126.com

Featured Application: This study aims to improve the design optimization of low Reynolds number propellers and the long-endurance capability of ultra-high-altitude unmanned aerial vehicles.

Abstract: Ultra-high-altitude unmanned aerial vehicles have created a high demand for the performance of propellers under low Reynolds numbers, while the efficiency of such propellers by the existing design framework has reached a bottleneck. This paper explores the possibility of extending the Gurney flap on low Reynolds number propellers to achieve efficiency breakthrough. An iterative optimization strategy for propellers with Gurney flaps is established, in which cross-sectional airfoils can be continuously optimized under updated Reynolds numbers and lift coefficients. A computational fluid dynamics (CFD) simulation based on the γ-Re_θ model was used as an aerodynamic analysis method. Propellers with and without Gurney flaps were optimized successively. Optimal results were analyzed using the CFD method. Results showed that an optimal propeller with a Gurney flap can achieve an efficiency of 82.0% in cruising conditions, which is 1.8% higher than an optimal propeller without a Gurney flap. Compared with the latter, the consumed power of the optimal propeller with a Gurney flap can be reduced by 2.2% with the same advance speed. Furthermore, the variation of the improvement by the Gurney flap propeller, along with its Reynolds number, was studied. A wind tunnel test indicates that the performance of the propellers obtained by the CFD method are in good agreement with the test results.

Keywords: low Reynolds number propeller; gurney flap; aerodynamic optimization; wind tunnel test; ultra-high-altitude unmanned aerial vehicle

Citation: Yao, Y.; Ma, D.; Zhang, L.; Yang, X.; Yu, Y. Aerodynamic Optimization and Analysis of Low Reynolds Number Propeller with Gurney Flap for Ultra-High-Altitude Unmanned Aerial Vehicle. *Appl. Sci.* **2022**, *12*, 3195. https://doi.org/10.3390/app12063195

Academic Editor: Seong-Ik Han

Received: 3 March 2022
Accepted: 20 March 2022
Published: 21 March 2022

1. Introduction

Ultra-high-altitude UAVs have significant advantages in cruising altitude, endurance, and long-term fixed-point parking [1,2]. Therefore, they have garnered considerable research attention in both military and civilian applications. Due to the difficulty in energy supply, ultra-high-altitude UAVs commonly use solar panels and batteries to supply power, and brushless motors are used to drive the propeller to provide thrust. Since the balance of energy is quite weak, the efficiency of the propeller is one of the key factors for ultra-high-altitude UAVs to survive day and night [3]. Complex environmental characteristics are the main challenge for the propeller design of ultra-high-altitude UAVs [4]. Because of the low air density (0.0889 kg/m^3 at 20 km altitude) and low cruising velocity (0.1 Ma) at high altitudes, the working Reynolds number of the propeller is lower than 1×10^5. Because of the influence of the low Reynolds number, the aerodynamic efficiency of such a propeller may be far lower than a conventional propeller, resulting in greater power consumption [5]. Therefore, improving the aerodynamic performance of low Reynolds number propellers is of great significance to enhance the long-endurance capability of ultra-high-altitude UAVs.

Generally, the performance of a propeller can be improved by reducing the induced loss of the blade and increasing the lift-to-drag ratio of the cross-sectional airfoil [6]. Based on the minimum energy loss principle, which is also known as the Betz optimum condition, and the blade element momentum theory (BEMT), Adkins et al. [7] proposed a fast propeller design method. Once the required thrust, rotational velocity, and diameter of the propeller were known, a design with minimum induced loss could be quickly achieved. Coupled with the free form deformation method, dynamic mesh interpolation technology, optimization algorithm, and surrogate model, YU et al. [8] developed an integrated aerodynamic and aeroacoustic design method of a propeller. Toman et al. [9] proposed an efficient optimization method of a propeller with a minimal number of high-fidelity model evaluations. In his method, the classical blade–element momentum theory and a high-fidelity computational fluid dynamics tool were linked by a space mapping algorithm to improve computing efficiency, but the blade cross-sectional airfoil was not optimized. Based on the hierarchical Kriging model, Bu et al. [10] proposed an aerodynamic/aeroacoustic optimization method in the design of a helicopter rotor and achieved considerable reduction in noise without compromising aerodynamic performance. Considering the influence of a low Reynolds number and its variation along the radial direction in experimental data, García-Gutiérrez et al. [11] designed a low Reynolds number propeller for a stratospheric airship adopting NACA4412 as the cross-sectional airfoil. Compared with the traditional method, the efficiency of the propeller was improved by 5%. The existing propeller design methods provide a rich reference for the construction of optimization methods for low Reynolds number propellers.

When a propeller is working at a very low Reynolds numbers, laminar separation bubbles can be easily generated on the blade and result in a significant drop in the propeller's efficiency. In order to accurately capture the effects of laminar bubbles on the performances of cross-sectional airfoils and blades, a high-precision CFD simulation method that can consider laminar transition is necessary in the optimization of low Reynolds number propellers [12]. The flow behavior on the blade is closely related to the aerodynamic characteristics of the propeller's cross-sectional airfoil at very low Reynolds numbers [13,14]. Thus, in the design of a low Reynolds number propeller, the aerodynamic performance of cross-sectional airfoils is more important [15,16] than that in a conventional propeller. Therefore, on the basis of existing propeller design methods, a more in-depth and detailed optimization of the cross-sectional airfoils at low Reynolds number may help to further improve the aerodynamic efficiency of such propellers. A Gurney flap is a flat, vertically mounted plate at the airfoil edge with a height of approximately 0.5% to 5% chord, which can contribute to lift enhancement by increasing the pressure of the lower surface, and can also bring about additional drag [17]. Giguere et al. [18] found that a Gurney flap can lead to significant enhancement in the lift and lift-to-drag ratio of airfoil at low speeds. Vijgen et al. [19] found both the solid and serrated Gurney flaps can increase the maximum lift-to-drag ratio of the wing by wind tunnel investigations. Traub and Akerson [20] studied the aerodynamic performance of an S8036 airfoil with a Gurney flap by a wind tunnel test. The results showed that the Gurney flap could significantly increase the maximum lift coefficient and the endurance parameters of the S8036 at Reynolds numbers of 4×10^4–8×10^4. Li et al. [21] studied the aerodynamic characteristics of an NACA0012 with a Gurney flap by wind tunnel test at a Reynolds number of 2×10^6. They found that the Gurney flap of all investigated heights (0.5–3%) could increase the lift-to-drag ratio when the lift coefficient was above 1.2. Zhu et al. [22] improved the flapping wing efficiency by the application of an adaptive Gurney flap. Woodgate et al. [23] demonstrated the implementation and use of Gurney flaps on wings and rotors. Motta et al. [24] applied a Gurney flap to the rotor blade and achieved vibration reduction. Based on the above research, it can be deduced that the application of a Gurney flap to the design of a cross-sectional airfoil has the possibility to help break through the efficiency bottleneck of low Reynolds number propellers. Since the aerodynamic performance of the airfoil is very sensitive to working conditions at low Reynolds numbers, it is better to optimize each cross-sectional airfoil with a Gurney flap

under corresponding actual working conditions. However, in the existing methods, the cross-sectional airfoils are not optimized under the actual working Reynolds numbers and lift coefficients determined by the cruise state of the designed propeller. This is because in the traditional non-iterative method, the design parameters and working status of the propeller are temporarily unavailable during the optimization of the cross-sectional airfoil, which can only be obtained after completing the optimization of chord and pitch distributions of the propeller. Therefore, the iterative optimization is necessary in the design of the low Reynolds number propellers.

In this study, an optimization method of creating a propeller with a Gurney flap for ultra-high-altitude UAV is established to weaken the adverse influence of low Reynolds numbers, and to research the general law of such a design. The rest of this paper is organized as follows. In Section 2, the aerodynamic analysis methods are introduced and validated. In Section 3, the proposed iterative optimization strategy for a low Reynolds number propeller with a Gurney flap is established. In each iteration of the optimization process, all the cross-sectional airfoils can be optimized under the Reynolds numbers and lift coefficients that are determined by the design state of the propeller obtained from last iteration. The CFD method based on the γ-Re_θ model, class-shape transformation method, polynomial interpolation method, and genetic algorithm were used to establish an iterative optimization platform. In Section 4, a propeller with a Gurney flap and a propeller without a Gurney flap were optimized by the proposed method for an ultra-high-altitude UAV. After that, a wind tunnel test was carried out to validate the optimization results. Then, a comparative analysis of the two optimized propellers was performed under different Reynolds numbers. Finally, the study is concluded in Section 5.

2. Numerical Method and Validation

In this study, the CFD method was used to realize high-fidelity calculations of the airfoil and propeller [25]. Reynolds-averaged Navier Stokes (RANS) equations were the governing equations, and finite volume method and second-order upwind scheme were used.

Since the propeller in this study worked at a low Reynolds number (10^4–10^5 level), laminar transition had to be taken into account in the numerical calculation. The γ-Re_θ model proposed by Menter and Langtry [26,27] was adopted as the transition model, which combines the advantages of the γ-Re_θ transition formula and the shear stress transport (SST) k-ω turbulence model. This model incorporates two additional transport equations of the local-transition Reynolds number $\widetilde{Re}_{\theta t}$ and the intermittent factor γ. The γ-Re_θ model is widely used in the calculation of low Reynolds number flow problems.

To precisely capture the transition boundary layers, $y+$ of the calculation grid was considered to be close to 1 [28]. The expression of $y+$ is as follows:

$$y^+ = \frac{\sqrt{\tau_\omega / \rho} \cdot \Delta y}{v} \quad (1)$$

where τ_ω is the shear stress of the wall, Δy is the height of the first grid cell off the wall, and v is kinematic viscous coefficient [29].

To verify the accuracy of this numerical calculation method for airfoil, the aerodynamic data of an Eppler 387 airfoil at different angles of attack under Re = 1.0×10^5 were calculated. The results were then compared with the experimental results from a low turbulence pressure tunnel (LTPT) at the Langley research center [30]. The test conditions and parameters of the test model are displayed in Table 1, where *Span* and *c* are the chord and span length of the test wing segment, *Ma* is the Mach number, *P* is the air pressure, and *Re* is the Reynolds number. More detailed information about the test model and the test method of Eppler 387 are introduced in [30] The computation grid of Eppler 387 is displayed in Figure 1. As shown in Figure 2, both the force coefficients and the laminar separation location calculated by CFD are in good agreement with the experimental results, which proves that this CFD method has high calculation accuracy for the aerodynamic characteristics of airfoil at low Reynolds numbers.

Table 1. Test conditions and parameters of the test model.

Span (m)	*c* (m)	*Ma*	*P* (kPa)	*Re*
0.9144	0.1524	0.05	34.475	1.0×10^5

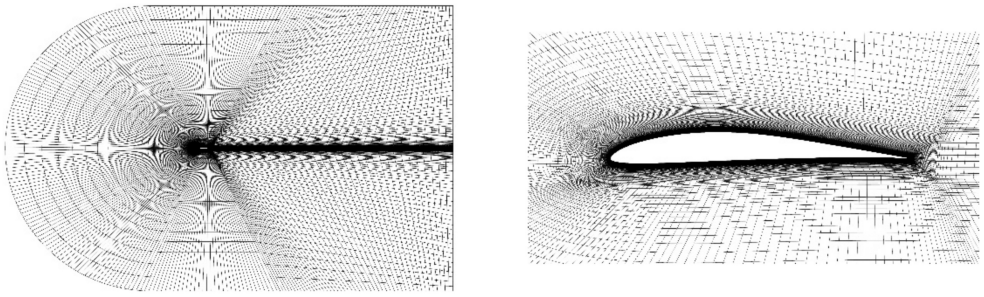

(**a**) (**b**)

Figure 1. Computation grid of Epller387: (**a**) Computational domain; (**b**) Near-wall grids distribution.

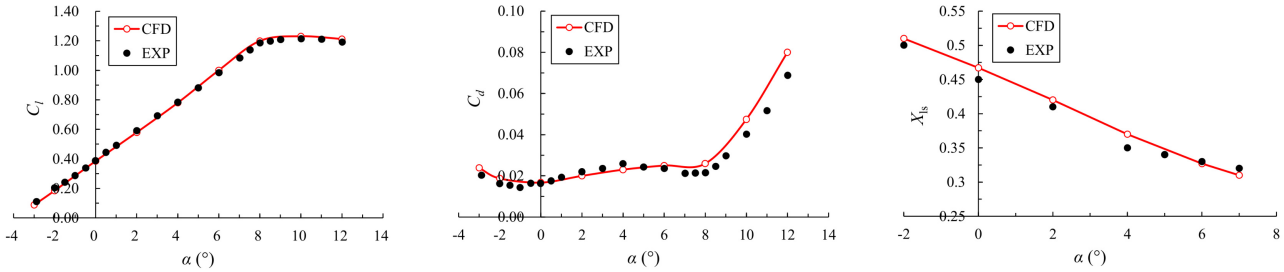

(**a**) (**b**) (**c**)

Figure 2. CFD and experimental results for Eppler 387 at $Re = 1.0 \times 10^5$: (**a**) Lift coefficient vs. angle of attack; (**b**) Drag coefficient vs. angle of attack; (**c**) Laminar separation location vs. angle of attack.

To verify the accuracy of this numerical calculation method for low a Reynolds number propeller, a propeller designed for a near-space solar-powered drone was selected for testing [31]. Figure 3 shows the chord and pitch distributions of the test propeller, and Figure 4 presents the three-dimensional shape of the test propeller. According to similarity criterion of equal Reynolds number and equal advance ratio (λ), ground experiments for the designed propeller, including thrust and torque measurement at a Reynolds number of about 1.7×10^5, were carried out [31]. The relation between test states on the ground and flight states at different altitudes are displayed in Table 2, where λ is the advance ratio, V_∞ is the free-stream velocity, n is the propeller rotational speed (revolutions per minute), and Re_{average} is the average Reynolds number of the blade sections of the propeller. In the test, the advance velocity of the propeller is controlled by a high accuracy railcar, as shown in Figure 5. More detailed information about the test propeller and the test method are introduced in [31].

The grid used for the calculation of the propeller is displayed in Figure 6. The radius of the propeller was R, and the distance from the front boundary of computational domain to the propeller was 12 R. The distance between the back boundary of the computational domain and the propeller was 24 R, and the distances from the out boundary to the rotation axis of the propeller were 6 R. To test the mesh independence, five grids of the same propeller with different densities were used to calculate aerodynamic characteristics at 10 km altitude when the free-stream velocity was 14.1 m/s and the rotational velocity per minute (n) was 622 rpm. The information of the five grids is shown in Table 3. Figure 7 shows that the calculation results tended to be stable with the increase in grid density. The thrust coefficient (C_T) and power coefficient (C_P) of Grid 1 and Grid 2 are far from stable

values. The calculation results of Grid 4 and Grid 5 are very close to the stable values. Thus, considering the computational cost and accuracy, Grid 4 was adopted.

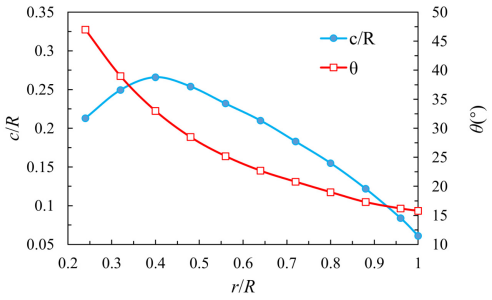

Figure 3. Chord and pitch distributions of the test propeller.

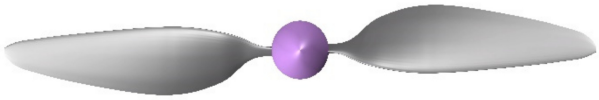

Figure 4. Three-dimensional shape of the test propeller.

Table 2. Relation between the test states and flight states of the test propeller.

Altitude (km)	λ	$Re_{average}$	Flight States		Test States	
			V_∞ (m/s)	n (rpm)	V_∞ (m/s)	n (rpm)
10	0.78	1.55×10^5	14.1	542	5.84	225
	0.68	1.73×10^5		622		258
	0.58	1.98×10^5		729		302

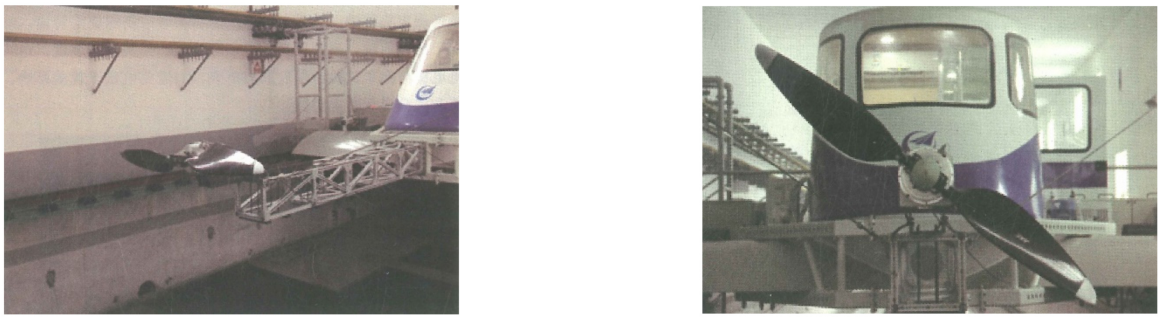

Figure 5. Ground experiment of the test propeller.

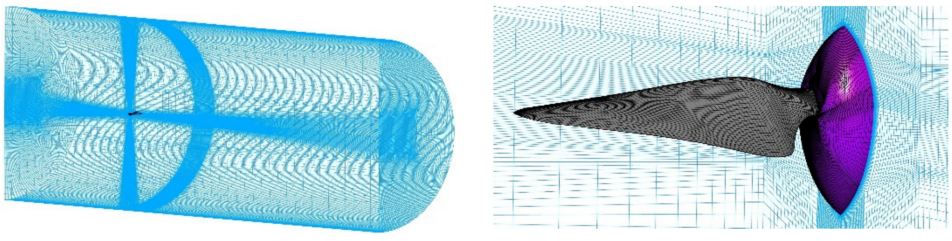

(**a**) (**b**)

Figure 6. Computational mesh of the test propeller: (**a**) Computational domain; (**b**) Near-wall grids distribution.

Table 3. Test conditions and parameters of the test model.

Grid	Number of Spanwise Nodes	Number of Chordal Nodes	Number of Cells
Grid 1	60	15	2.16×10^6
Grid 2	80	30	2.98×10^6
Grid 3	100	45	3.87×10^6
Grid 4	120	60	5.22×10^6
Grid 5	140	75	6.91×10^6

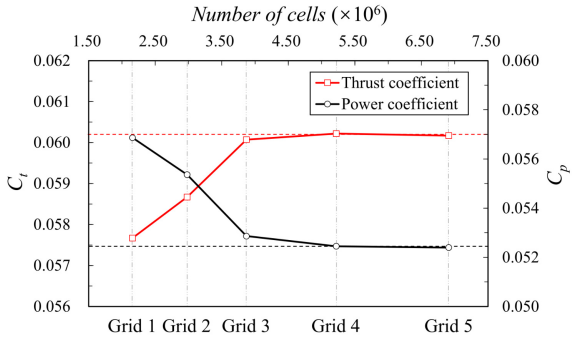

Figure 7. Comparison of calculation results of five grids.

The aerodynamic performances of the propeller calculated by the CFD method were compared with the experimental results in Figure 8. The results show that the thrust coefficient (C_T), power coefficient (C_P), and efficiency (η) calculated by the CFD are close to the experimental results. Therefore, the computational fluid dynamics (CFD) simulation based on the γ-Re_θ model has sufficient accuracy for the performance calculations of airfoil and propeller at low Reynolds numbers. In this study, it was used to evaluate the performance of the cross-sectional airfoil and propeller during the optimization process.

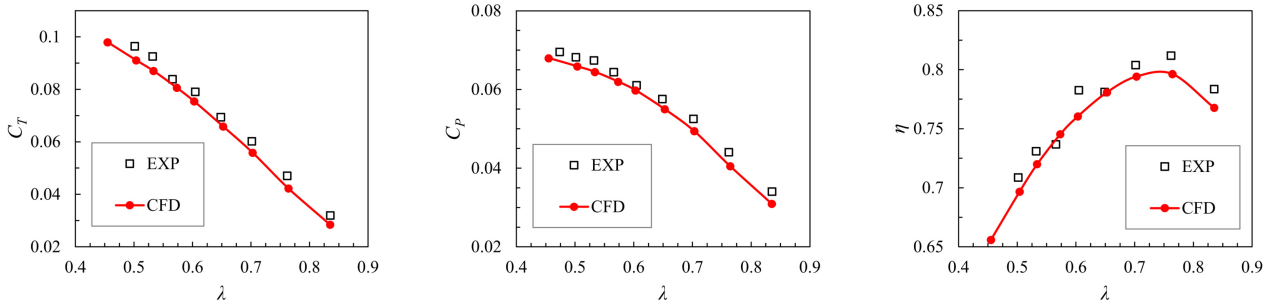

Figure 8. Experimental data and CFD results at an altitude of 10 km: (**a**) Thrust coefficient vs. advance ratio; (**b**) Power coefficient vs. advance ratio; (**c**) Propeller efficiency vs. advance ratio.

3. Optimization Strategy

In this part, an optimization strategy for a low Reynolds number propeller with a Gurney flap is proposed, which involves iterative optimization of cross-sectional airfoils and of chord and pitch distributions. Different from the traditional design method of low Reynolds number propellers, the proposed method can optimize the cross-sectional airfoils under a specific Reynolds number and lift the coefficient determined by the actual working conditions and shape of the propeller obtained from the last iteration. In addition, a computational fluid dynamics (CFD) simulation based on the γ-Re_θ model was used as the aerodynamic analysis method in the optimization. The establishment of the iterative optimization platform for a low Reynolds number propeller is described below.

3.1. Optimization Model of Cross-Sectional Airfoil with Gurney Flap

In the iterative optimization of a low Reynolds number propeller, each cross-sectional airfoil needs to be optimized under corresponding constraints which are constantly updated with the iteration. The optimization process of a cross-sectional airfoil with a Gurney flap is introduced in this subsection.

Firstly, the upper and lower curves of the airfoil were parameterized by the class-shape transformation (CST) method [32]. Two 4th order curves controlled by the parameters a_0–a_4 and b_0–b_4 were used to describe the airfoil, which can be expressed as follows:

$$\begin{cases} C_{upper}(\overline{x}) = \overline{x}^{N_1}(1-\overline{x})^{N_2}\sum\limits_{i=0}^{4} a_i B_4^i(\overline{x}) \\ C_{lower}(\overline{x}) = \overline{x}^{N_1}(1-\overline{x})^{N_2}\sum\limits_{i=0}^{4} b_i B_4^i(\overline{x}) \\ B_4^i(\overline{x}) = \frac{4!}{i!(4-i)!}\overline{x}^i(1-\overline{x})^{4-i}, i = 0, 1, \ldots, 4 \end{cases} \quad (2)$$

where $N_1 = 0.5$ and $N_2 = 1$ represent an airfoil with a round head and a pointed tail, and the parameters a_i and b_i are the weight coefficients of Bernstein polynomials $B_n^i(\varphi)$. In addition, $\overline{x}$ is the dimensionless chordwise position on the airfoil chord, which is expressed by x/c.

Further, the relative height of the Gurney flap to the airfoil chord on the Gurney flap airfoil is expressed by $\overline{h} = h/c$, which is given and fixed in the airfoil optimization to avoid the irregular shape of the propeller trailing edge (such as a wavy shape). When $\overline{h}$ is 0, the airfoil degenerates into a conventional airfoil without a Gurney flap. Therefore, there are a total of ten design variables in the optimization of the cross-sectional airfoil, as shown in Figure 9.

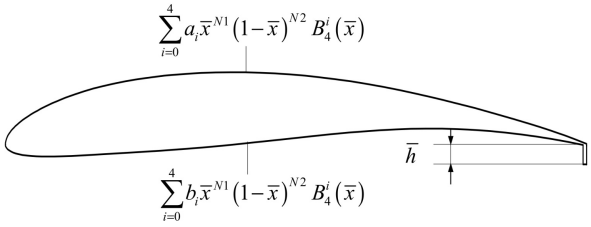

Figure 9. Parametric method for a Gurney flap airfoil.

Then, the constraints and optimization objective of the cross-sectional airfoil are determined as follows:

(a) Constraint of cross-sectional airfoil's relative thickness

The variation in the relative thickness distribution of the blade usually depends on the structural strength requirements. Here, the relative thickness (t_{target}) distribution of the propeller is constrained as follows:

$$t_{\text{target}} = 0.481\left(\frac{r}{R}\right)^4 - 1.616\left(\frac{r}{R}\right)^3 + 2.036\left(\frac{r}{R}\right)^2 - 1.143\frac{r}{R} + 0.305 \quad (3)$$

where t_{target} is the ratio of the actual thickness to the chord length of the airfoil, and r is the radial position of the blade element.

(b) Constraint of the cross-sectional airfoil's lift coefficient

The lift coefficient distribution of the cross-sectional airfoils should be constrained by the working state of the designed propeller. In the iterative optimizations, the chord and pitch distributions can be obtained after the first iteration. Then the lift coefficient

distribution ($C_{l\text{-target}}$) of the propeller at a working state can be calculated by blade element momentum theory [33] (BEMT) as follows [34]:

$$C_{l\text{-target}} = \frac{4\sin(\varphi_0 + \beta)\tan\beta}{\sigma(1 - K^{-1}\tan\beta)} \tag{4}$$

where β is the induced angle which can be solved by Newton iterative method, K is the ratio of lift coefficient to drag coefficient of a local blade element, and σ is the local blade solidity which is expressed by:

$$\sigma = \frac{N_B c}{2\pi r} \tag{5}$$

where N_B is the number of propeller blades.

$C_{l\text{-target}}$ is used as the aerodynamic constraint in the optimization of cross-sectional airfoils.

(c) Constraint of cross-sectional airfoil's working Reynolds number

Each cross-sectional airfoil must be optimized under the corresponding Reynolds number (Re_{target}) determined by the working status of the propeller. The Reynolds number of each cross-sectional airfoil on the propeller can be expressed as follows:

$$Re_{\text{target}} = \frac{\rho c\sqrt{{V_\infty}^2 + (2\pi n_s r)^2}}{\mu} \tag{6}$$

where μ is the dynamic viscosity coefficient at the cruise state of the propeller.

(d) Objective function of the cross-sectional airfoil optimization

The aim of airfoil optimization is to maximize the efficiency of each blade element. The efficiency of blade element can be expressed as follows:

$$\eta_{\text{element}} = \frac{\mathrm{d}T \cdot V_\infty}{\mathrm{d}F \cdot 2\pi n_s r} \tag{7}$$

As shown in Figure 10, the thrust (dT) and rotational drag (dF) of each blade element can be expressed by the lift (dL) and drag (dD) as follows:

$$\begin{cases} \mathrm{d}T = \mathrm{d}L\cos\varphi - \mathrm{d}D\sin\varphi \\ \mathrm{d}F = \mathrm{d}L\sin\varphi + \mathrm{d}D\cos\varphi \end{cases} \tag{8}$$

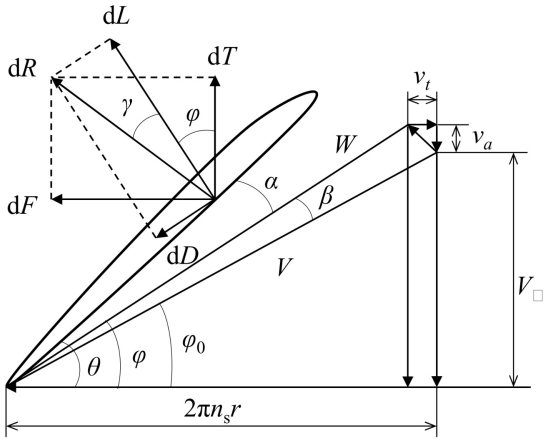

Figure 10. Force diagram for a blade element.

Then, the efficiency of each blade element can be written as

$$\eta_{\text{element}} = \frac{K\cos\varphi - \sin\varphi}{K\sin\varphi + \cos\varphi} \cdot \tan\varphi_0 \tag{9}$$

It can be proved by calculating the derivative function of Equation (9) with respect to K that when φ and φ_0 are known, η_{element} is a monotonically increasing function of K. It indicates when K gets the maximum value, η_{element} will also get the maximum value. So, the lift-to-drag ratio K was used as the objective function in the optimization of the corresponding cross-sectional airfoil.

Thus, the optimization model of the cross-sectional airfoil can be constructed as follows:

$$\begin{array}{ll} \text{find} & \boldsymbol{x} = [\, a_0, \cdots, a_4, b_0, \cdots, b_4] \\ \max & K \\ \text{s.t.} & Re = Re_{\text{target}} \\ & C_l = C_{l\text{-target}} \\ & t = t_{\text{target}} \end{array} \tag{10}$$

To ensure the accuracy of the design results, the CFD method based on the γ-Re_θ model was used to calculate the aerodynamic data of the cross-sectional airfoil with a Gurney flap in the optimization. In addition, the computation grid of the airfoil can be automatically updated with the change of the shape (see Figure 11). The results of the grid dependency study of the airfoil with a Gurney flap show that when the number of cells increases to 42,000, the aerodynamic characteristics of the airfoil become stable and hardly change with the increase in the number of cells. Taking the calculation accuracy and calculation efficiency into consideration, the size of the computational grid used for calculation is set at 54,000.

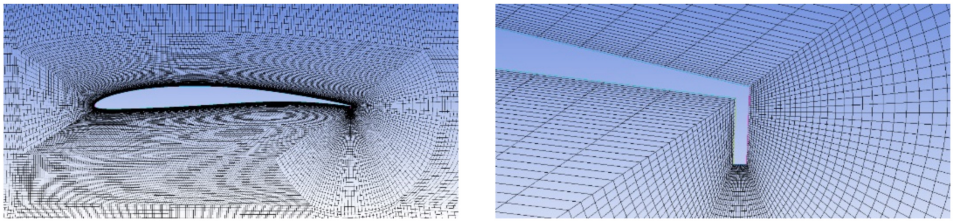

(**a**) (**b**)

Figure 11. Computation grid of the cross-sectional airfoil with a Gurney flap: (**a**) Grid around the airfoil; (**b**) Grid near the Gurney flap.

3.2. Optimization Model of Propeller Chord and Pitch Distributions

Based on the optimization results of cross-sectional airfoils, the chord and pitch distributions of the propeller can be optimized. The chord and pitch distributions of the blade were parameterized by two 2nd order CST curves and were respectively controlled by parameters c_0–c_2 and d_0–d_2, which can be expressed as follows:

$$\begin{cases} c(\bar{r}) = \bar{r}^{N_1}(1-\bar{r})^{N_2}\sum\limits_{i=0}^{2} c_i B_2^i(\bar{r}) + (1-\bar{r})\cdot(c_{\text{start}} - c_{\text{end}}) + c_{\text{end}} \\ \theta(\bar{r}) = \bar{r}^{N_1}(1-\bar{r})^{N_2}\sum\limits_{i=0}^{2} d_i B_2^i(\bar{r}) + (1-\bar{r})\cdot(\theta_{\text{start}} - \theta_{\text{end}}) + \theta_{\text{end}} \\ B_2^i(\bar{r}) = \frac{2!}{i!(2-i)!}\bar{r}^i(1-\bar{r})^{2-i}, i = 0,1,2 \end{cases} \tag{11}$$

where N_1 and N_2 use the same values as in Equation (4), $\bar{r}$ is the dimensionless radial position on the blade, and is expressed by r/R. c_{start} and c_{end} are the chord at $\bar{r} = 0$ and $\bar{r} = 1$, and θ_{start} and θ_{end} are the pitches at $\bar{r} = 0$ and $\bar{r} = 1$.

To avoid unreasonable design and reduce the variables, c_{start} and c_{end} were given and fixed during the optimization. θ_{start} and θ_{end} were used as optimization design variables.

Therefore, there were a total of eight design variables in the optimization of the propeller chord and pitch distributions. Besides, since the hub of the blade has a minor influence on the propeller performance, Gurney flaps were only used on the blade in the radial range of 0.2 R–1.0 R. According to the given values of the parameters c_0–c_2, d_0–d_2, θ_{start}, and θ_{end}, the chord and pitch values at 17 radial positions could be calculated. Then, the three-dimensional shape of the propeller with a Gurney flap could be obtained, as shown in Figure 12.

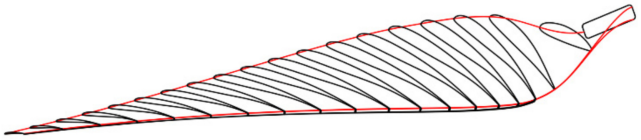

Figure 12. Parametric method for the propeller with a Gurney flap.

Then, similar to the airfoil optimization, the constraints and objective function for optimization of propeller were determined as follows:

(a) Constraint of propeller's structural mass.

To limit the structural mass of the propeller, the structural form, in which high modulus carbon fiber cloth was wrapped around the rigid foam core, was adopted. The mass of the propeller m can be estimated as follows:

$$m = S_{\text{prop}} e \rho_c + (V_{\text{prop}} - S_{\text{prop}} e) \rho_f \tag{12}$$

where S_{prop} is the wetted area of the propeller, e is the thickness of the carbon fiber cloth, ρ_{c} is the volume density of the carbon fiber cloth, V_{prop} is the volume of the propeller, and ρ_{f} is the volume density of the rigid foam.

(b) Constraint of propeller's required thrust.

The aim of the propeller optimization was to maximize the efficiency at the required thrust (T_{req}). Polynomial interpolation method was used to calculate the propeller rotational velocity and aerodynamic efficiency at T_{req}. Firstly, the thrusts T_1, T_2, and T_3 corresponding to three different rotational velocities n_{s1}, n_{s2}, and n_{s3} could be calculated. Then, according to these three sets of data, a quadratic polynomial function could be fitted as $T = T(n_s)$. Finally, the rotational velocity $n_{s\text{-req}}$ corresponding to the required thrust T_{req} could be solved with the equation $T_{\text{req}} = T(n_{s\text{-req}})$.

(c) Objective function for the optimization of chord and pitch distributions.

The aim of the optimization is to maximize the efficiency (η_{req}) at the required thrust (T_{req}), which can be calculated as follows:

$$\eta_{\text{req}} = \frac{T_{\text{req}} V_\infty}{2\pi n_{s\text{-req}} Q_{\text{req}}} \tag{13}$$

where Q_{req} is the propeller torque corresponding to T_{req}.

In summary, the optimization model of chord and pitch distributions can be described as follows:

$$\begin{array}{ll} \text{find} & \boldsymbol{x} = [\, c_0, c_1, c_2, d_0, d_1, d_2, \theta_{\text{start}}, \theta_{\text{end}}] \\ \max & \eta_{\text{req}} \\ s.t. & m \le m_{\max} \\ & T = T_{\text{req}} \end{array} \tag{14}$$

where $m_{\max}$ is the allowable maximum structural mass of the propeller.

The CFD method is applied to the optimization of the propeller to evaluate the performance under low Reynolds number, and the computation grid of the propeller can be updated with the change of the propeller through the automatic adjustment blocks around the propeller, as shown in Figure 13.

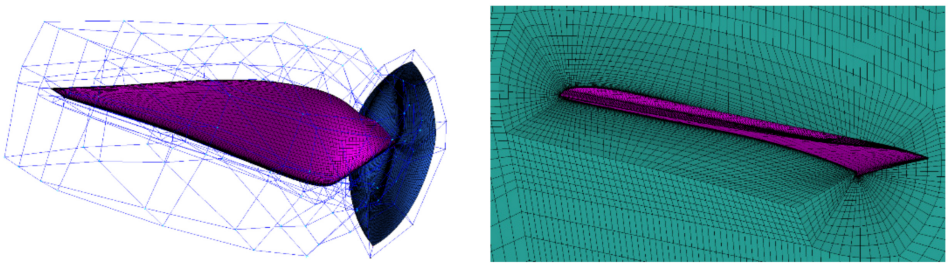

(**a**) (**b**)

Figure 13. Computation grid of the propeller with a Gurney flap: (**a**) Adjustable blocks around the propeller; (**b**) Grid around cross-sectional airfoil with a Gurney flap.

3.3. Iterative Optimization Method for Low Reynolds Number Propeller with Gurney Flap

To obtain the optimal performance of the cross-sectional airfoils, each airfoil with a Gurney flap needs to be optimized under a specific Reynolds number and the lift coefficient determined by the actual working conditions of the propeller. However, in the traditional design method of conventional propellers, the Reynolds number and lift coefficient of the cross-sectional airfoil are unavailable before the design is completed. This problem can be solved by the iterative optimization of the cross-sectional airfoils and the chord and pitch distributions. The procedure for the iterative optimization strategy for low Reynolds number propeller is described as follows:

Step 1. Input the initial design parameters

To start the optimization, the following parameters must be initialized:

(1) Free-stream velocity (V_∞);
(2) Propeller radius (R);
(3) Blade number (N_B);
(4) Required thrust (T_{req});
(5) Propeller rotation velocity (n_s);
(6) Aerodynamic data of the initial cross-sectional airfoils.

where the rotational velocity is only empirically given as n_s in this step, and will change into $n_{s\text{-req}}$ (the rotational velocity corresponding to the required thrust) after the optimization of the propeller in Step 4.

Step 2. Obtain the initial chord and pitch distributions by Betz method.

According to the given parameters in step 1, an initial propeller can be designed by the Betz method [7]. In addition, the initial chord and pitch distributions can be obtained.

Step 3. Optimize the cross-sectional airfoils with a Gurney flap.

Seventeen cross-sectional airfoils with a Gurney flap with an interval of 0.05 R in the radial range of 0.2 R–1.0 R on the blade were optimized according to the following steps:

(1) Firstly, the airfoil was parameterized by two 4th CST curves. In addition, the relative height of the Gurney flap for the Gurney flap airfoil was fixed as $\overline{h}$. The design space of the airfoil was composed of 10 variables (a_0–a_4 and b_0–b_4), from which the samples were generated. The constraints of the lift coefficient ($C_{l\text{-target}}$) and working Reynolds number (Re_{target}) of the airfoil were calculated according to the initial propeller in Step 2 in the first iteration. In addition, in the following iterations, they were obtained from Step 6.
(2) For each sample, the lift coefficients C_{l1} and C_{l2} at the angles of attack α_1 and α_2 were calculated by the CFD method. Then, the required angle of attack α_{target} corresponding to $C_{l\text{-target}}$ was obtained by linear interpolation. So, the lift-to-drag ratio K corresponding to α_{target} for each sample could be calculated.
(3) Multi-island genetic algorithm (MIGA) [29] was used to evaluate existed samples and generate new samples from the design space that potentially have bigger lift-to-drag ratios.
(4) Once the relative difference in the lift-to-drag ratio (K) between two adjacent samples was less than ε_1 for 20 consecutive times, the optimization was finished and the sample

with the maximum K was considered as the optimal solution. Otherwise, (2) and (3) needed to be repeated.

Step 4. Optimize the chord and pitch distributions of propeller.

(1) Firstly, the chord and pitch distributions were parameterized by two 2nd CST curves, respectively. In addition, the design space of the airfoil was composed of eight variables (c_0–c_2, d_0–d_2, θ_{start} and θ_{end}), from which the samples were generated.

(2) Using polynomial interpolation method, the rotational velocity (n_s-req), torque (Q_{req}), and efficiency (η_{req}) corresponding to the required thrust (T_{req}) of each sample could be calculated by the CFD method.

(3) Multi-island genetic algorithm was used to evaluate the existing samples and generate new samples from the design space that potentially had higher efficiencies.

(4) Once the relative difference in efficiency (η_{req}) of two adjacent samples was less than ε_2 for 20 consecutive times, the optimization was finished and the sample with the maximum η_{req} was considered as the optimal solution. Otherwise, (2) and (3) needed to be repeated.

Step 5. Judge whether the iterative optimization converges.

If the relative difference in η_{req} obtained in Step 4 between two adjacent iterations was less than ε_3, the whole optimization was finished and the propeller with maximum efficiency η_{req} in the last iteration was considered as the final optimal solution. Otherwise, we proceeded to Step 6.

Step 6. Update the constraints for the cross-sectional airfoils by BEMT method.

We constructed an aerodynamic response surface of the cross-sectional airfoils by polynomial interpolation of CFD data. Subsequently, according to the new chord, the pitch distributions and rotational velocity of the optimized propeller were obtained from step 4, and the lift coefficient (C_l-target) and working Reynolds number (Re_{target}) of each cross-sectional airfoil were updated. Then, we returned step 3 for the next iteration optimization.

The optimization procedure is summarized in Figure 14.

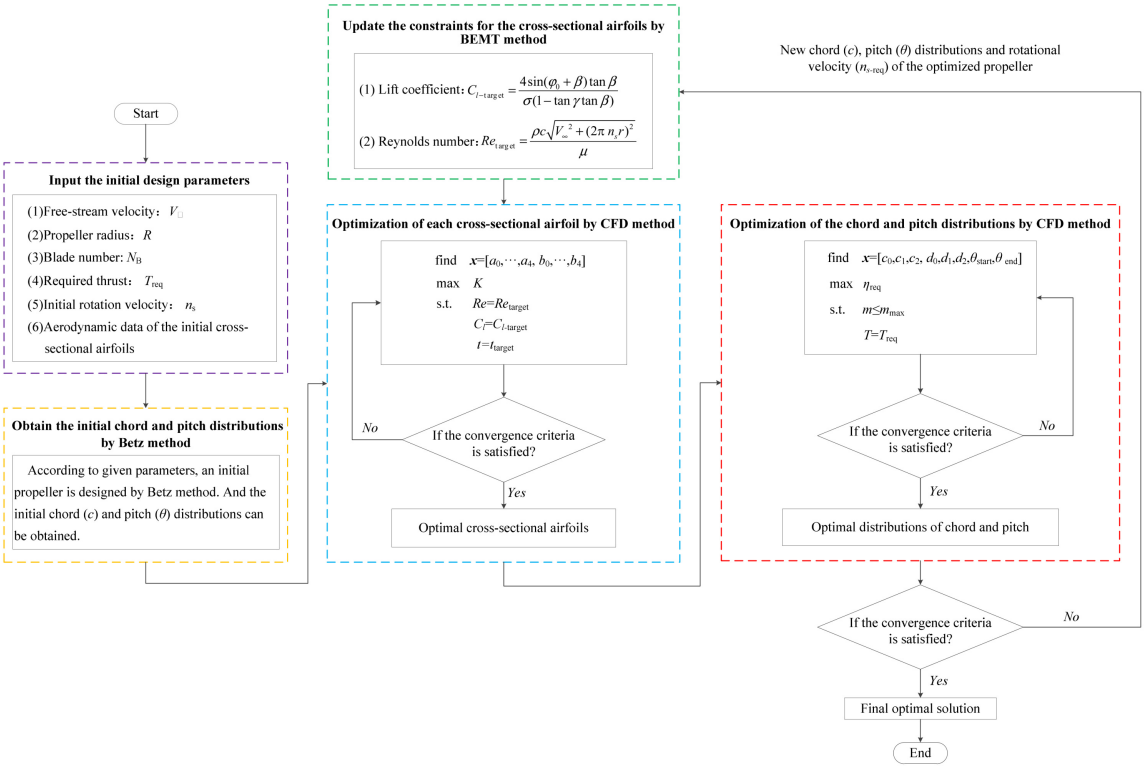

Figure 14. Flowchart of iterative optimization strategy for low Reynolds number propeller.

4. Case Study and Analysis

To validate the effectiveness of the proposed methodology, a propeller with a Gurney flap was designed for an ultra-high-altitude UAV (see Figure 15) working at an altitude of 20 km with a cruising velocity of 32 m/s. The fixed parameters and design state for the propeller are displayed in Table 4. The average working Reynolds number of the cross-sectional airfoils (Re_{average}) for the propeller was estimated lower than 6×10^4. The relative height of Gurney flap for the cross-sectional airfoil in the optimization of the Gurney flap propeller was taken as 1%. In order to quantify and analyze the effect of the Gurney flap on the aerodynamic performance of the propeller, a propeller without a Gurney flap was completed as a comparison, which was also designed by the proposed method by making the relative height of the Gurney flap on the cross-sectional airfoil be 0. In addition, the turbulence intensity used in the CFD calculations was set as 0.1%.

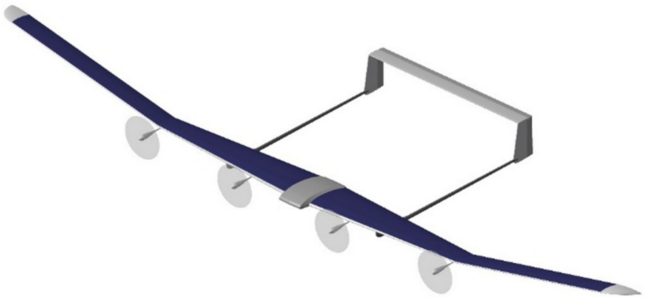

Figure 15. The ultra-high-altitude unmanned aerial vehicle for case study.

Table 4. Parameters of propeller and the design state.

N_B	D (m)	V_∞ (m/s)	P (kg/m^3)	μ (Ns/m^2)	T_{req} (N)
2	2	32	0.0889	1.422×10^{-5}	20

4.1. Optimization Results

The designs of the propeller with a Gurney flap and the propeller without a Gurney flap were completed after iterative optimization. Figure 16 shows the convergence histories of the chord and pitch distribution optimization for two propellers in the last iteration. For convenience, the optimized propeller without a Gurney flap is denoted by Prop A, and the optimized propeller with a Gurney flap is denoted by Prop B in this paper. Figure 17 shows the geometry of Prop A and Prop B, where the red part is a Gurney flap. Their chord and pitch distributions are displayed in Figures 18 and 19, respectively.

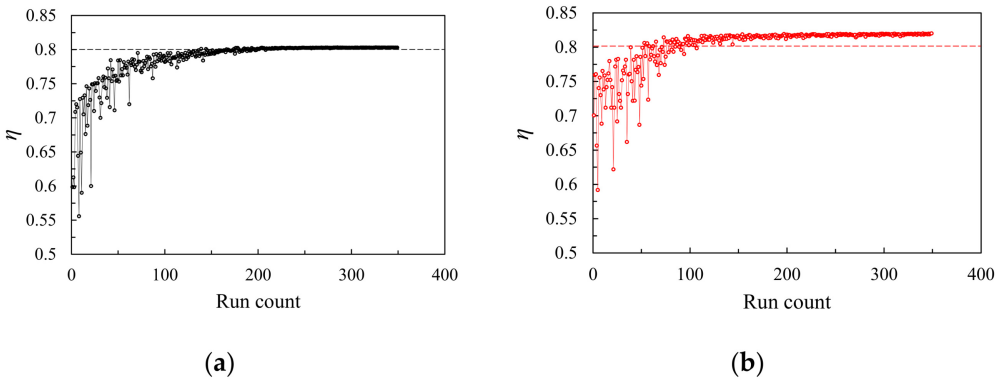

Figure 16. Convergence history of two optimized propellers in the optimization of chord and pitch distribution: (**a**) Prop A; (**b**) Prop B.

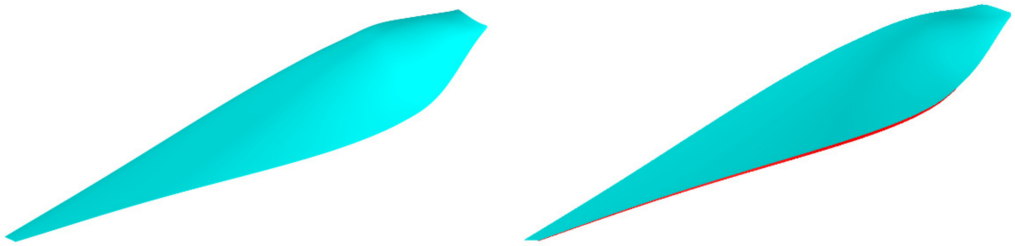

(**a**) (**b**)

Figure 17. The geometries of the optimized propellers: (**a**) Prop A; (**b**) Prop B.

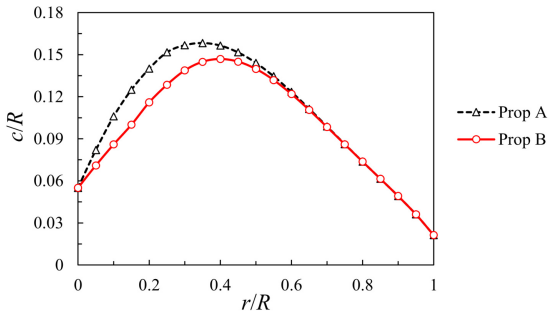

Figure 18. Blade chord distribution of the two optimized propellers.

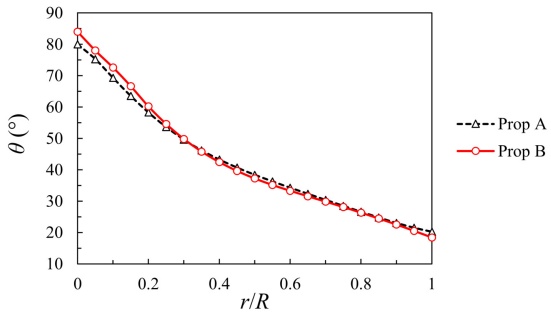

Figure 19. Blade pitch distribution of the two optimized propellers.

As shown in Table 5, Prop B (propeller with a Gurney flap) can achieve 1.8% higher efficiency than Prop A (propeller without a Gurney flap) under the required thrust at the design point. That means, compared with the optimal propeller without a Gurney flap, adopting the optimal propeller with a Gurney flap can reduce the output power of the ultra-high-altitude unmanned aerial vehicle by 2.2%. It is of great significance to enhance the long-endurance capability of the ultra-high-altitude UAV. Therefore, the optimization of the propeller with a Gurney flap has evident effects.

Table 5. Comparison between two optimized propellers at the design point.

Propeller	T_{req}(N)	n (rpm)	λ	η	$Re_{average}$
Prop A	20	978	0.9816	80.2%	4.2×10^4
Prop B	20	948	1.0105	82.0%	4.0×10^4

The aerodynamic performances of Prop A and Prop B near the design point were calculated, as shown in Figure 20. In addition, the average Reynolds numbers ($Re_{average}$) of the two propellers at different rotational velocities were in the range of 3.5×10^4 to 4.6×10^4. It can be seen that Prop B can maintain a significantly higher efficiency than Prop A in a wide range of thrusts near the design point. Thus, the improvement of the propeller with a Gurney flap is reliable.

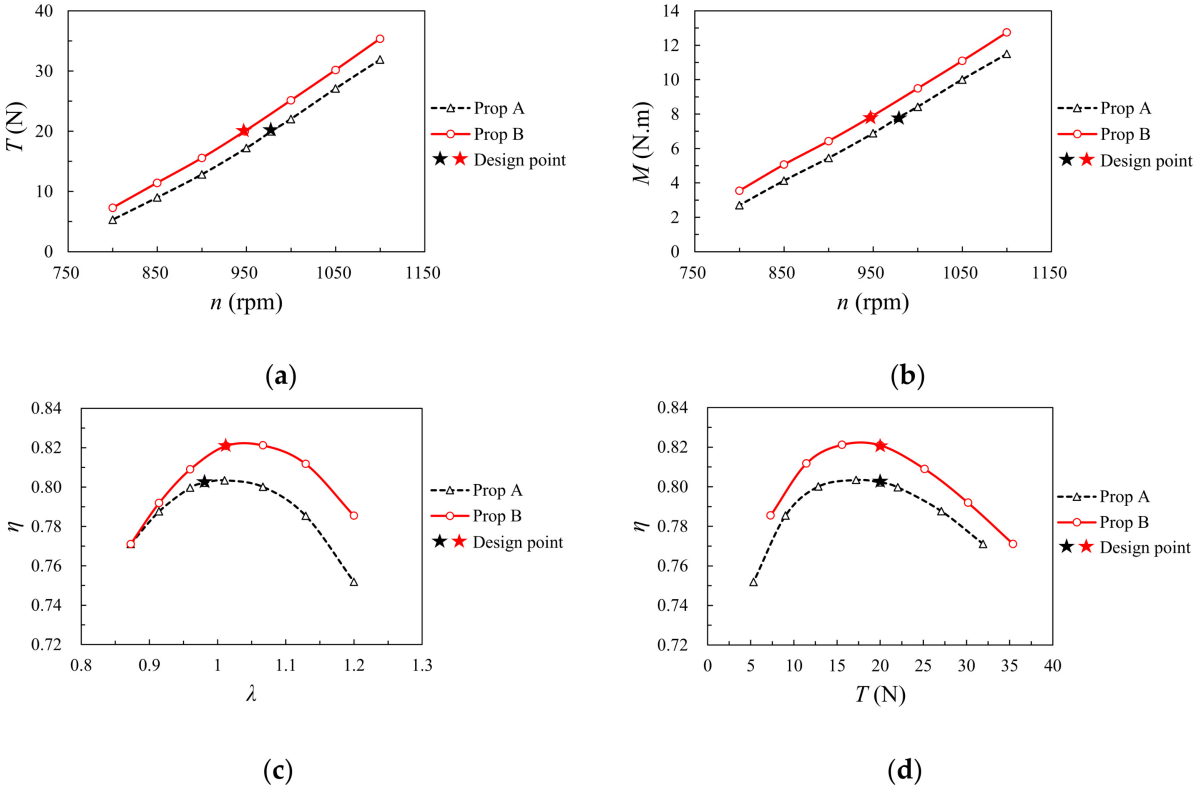

Figure 20. Aerodynamic performances of Prop A and Prop B near the design point: (**a**) Thrust vs. rotational velocity; (**b**) Torque vs. rotational velocity; (**c**) Efficiency vs. advance ratio; (**d**) Efficiency vs. thrust.

In addition, the aerodynamic performances of Prop A and Prop B under higher Reynolds numbers (about 1.8×10^5) were also calculated, as shown in Figure 21. The increase in Reynolds number is achieved by changing the air density and dynamic viscosity, and the rotational velocity of the propeller and free-stream velocity remain unchanged. The contrast point in Figure 21 is working state that has the same advance ration with the design point in Figure 20. It can be seen that both propellers can achieve more than 86% aerodynamic efficiency within this Reynolds number range, but Prop B no longer has higher aerodynamic efficiencies than Prop A near the contrast point. This indicates that Reynolds number may weaken the aerodynamic improvement of the propeller with a Gurney flap.

To explain the effect of Reynolds number, the efficiencies of Prop A and Prop B at five Reynolds numbers under were calculated, where the advance ratios of two propellers were consistent with their design cruise states. As shown in Figure 22, with the Reynolds number increasing, the efficiency improvement of Prop B relative to Prop A gradually decreases. In addition, as the Reynolds number increases to about 1.4×10^5, Prop B no longer has an efficiency advantage relative to Prop A.

4.2. Wind Tunnel Test

In this subsection, the aerodynamic performance of the optimized propellers with and without a Gurney flap were further studied by the force measurement test of their scaled models in the wind tunnel, and the computational fluid dynamics calculation method was verified.

4.2.1. Test Conditions and Method

The wind tunnel was a single return-flow and closed wind tunnel. In addition, its test section was 12 m long and its cross section was a 3×3 m rounded rectangle. The

turbulence intensity of this wind tunnel was 0.1–0.13%. In addition, the wind speed could be continuously controlled from 3–100 m/s. A sketch of wind tunnel is shown in Figure 23.

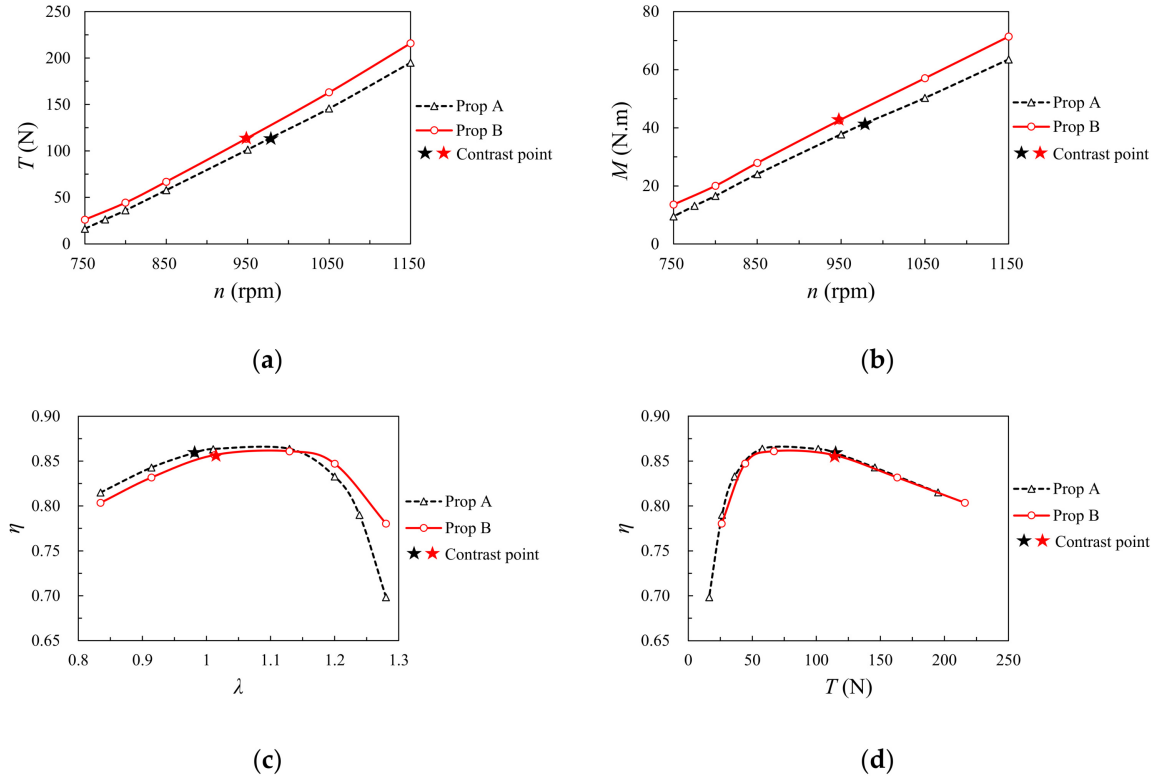

Figure 21. Aerodynamic performances of two optimized propellers under an average Reynolds number of about 1.8×10^5: (**a**) Thrust vs. rotational velocity; (**b**) Torque vs. rotational velocity; (**c**) Efficiency vs. advance ratio; (**d**) Efficiency vs. thrust.

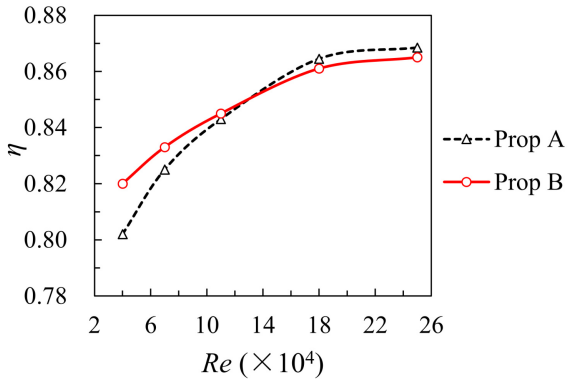

Figure 22. Aerodynamic performances of Prop A and Prop B at their design advance ratios.

In the wind tunnel test of propeller, the criteria of geometric similarity, kinematic similarity, and dynamic similarity were required for a model to have similitude with the prototype [35]. The thrust coefficient (C_T) and power coefficient (C_P) of the propellers can be expressed as follows:

$$\begin{aligned} C_T &= \frac{T}{\rho {n_s}^2 D^4} = f_T(\lambda, Re, Ma) \\ C_P &= \frac{P}{\rho {n_s}^3 D^5} = f_P(\lambda, Re, Ma) \end{aligned} \tag{15}$$

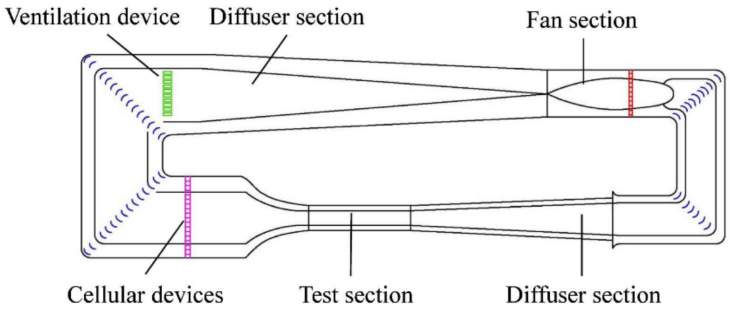

Figure 23. Wind tunnel.

Thus, the advance ratio, Reynolds number and Mach number of the test model needed to be the same as the prototype. In general, it is often impossible to strictly meet all requirements during a model test, so some unimportant aspects of similitude may be neglected [36]. In this study, the Mach number of the propeller tip was lower than 0.4 and could be ignored, and only the advance ratio (λ) and Reynolds number (Re) of the test models were guaranteed to be the same as that of the prototypes. Then the scaling laws of the free-stream velocity (V_∞) and rotational velocity (n_s) between the prototype and the test model could be formulated as follows:

$$\begin{array}{l} \frac{V_{\infty 1}}{V_{\infty 2}} = \frac{\rho_2 D_2}{\rho_1 D_1} \cdot \frac{\mu_1}{\mu_2} \\ \frac{n_{s1}}{n_{s2}} = \frac{V_{\infty 1}}{V_{\infty 2}} \cdot \frac{D_2}{D_1} \end{array} \quad (16)$$

where parameters with subscript $_1$ correspond to prototype, and parameters with subscript $_2$ correspond to test model.

The test models were made of carbon fiber and resin material using a high-precision steel mold, and the diameters of the models were 1.40 m, which was 0.7 times the diameter of Prop A and Prop B, as shown in Figures 24 and 25. The mass of the test models was controlled within 200 g, and their dynamic balance performances were qualified after inspection. The test model was installed in front of the force measurement device, and the measurement device was connected with an extended strut. The extended strut was mounted on the ground of the wind tunnel, as shown in Figure 26.

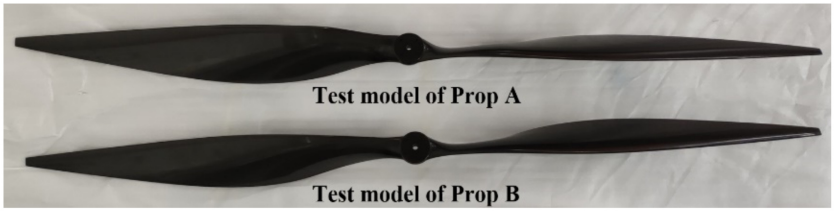

Figure 24. The test models.

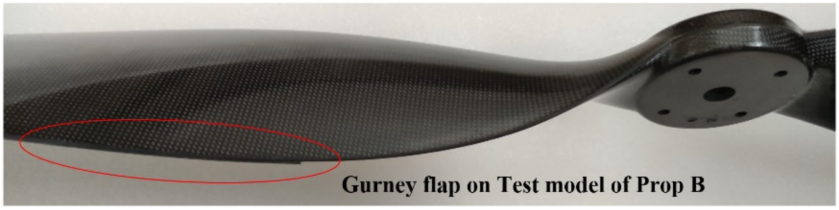

Figure 25. The detail of the Gurney flap on the test model.

(**a**) (**b**)

Figure 26. Test propellers installed in the wind tunnel: (**a**) The test propeller without a Gurney flap (Prop A); (**b**) The test propeller with a Gurney flap (Prop B).

In the wind tunnel test of the propeller, the maximum blockage was 2.1%, which met the requirement of wind tunnel test. Considering the blockage effect, the test results were corrected by the blockage correction method [37]. In order to check the accuracy of the test result under low Reynolds numbers, a repeated test was first carried out. The force measurement test of the scaled model of Prop A was performed three times under the same condition, where the Re was about 1.6×10^5 and the freestream velocity was 16 m/s. The data of each test state were obtained by averaging the results of 800 consecutive samples in steady state. As shown in Figure 27, the relative system error of three tests was within 1%, which satisfies the requirement of this study.

4.2.2. Results and Analysis of the Test

Two force measurement tests of the scaled model of Prop A and Prop B in different Reynolds number ranges were carried out, as shown in Table 6. One test was performed with a freestream velocity of 4.2 m/s ($Re_{\text{average}} \approx 4 \times 10^4$), which corresponded to the design point of the propeller. In addition, the other test was performed with a freestream velocity of 16 m/s, which corresponded to the working state of the propeller at a higher Reynolds number of about 1.6×10^5. Limited by the maximum measuring range of the force measurement device, tests under higher Reynolds numbers were not performed, but the results of these two tests were sufficient.

The comparison of the wind tunnel test and CFD results under $Re \approx 4 \times 10^4$ and $Re \approx 1.6 \times 10^5$ are shown in Figures 28 and 29, respectively. It can be seen that the thrust coefficient, power coefficient, and efficiency obtained from the wind tunnel test were slightly larger than the CFD results, which may be caused by the fact that the actual turbulence of the airflow at such low velocity in the test was larger than expected. However, the variation trend of performance data with advance ratio by CFD method is consistent with the results of the wind tunnel test. Besides, as shown in Figure 28, the propeller with a Gurney flap had about 1% higher efficiency at the advance ratio of about 1.0 than that of the propeller without a Gurney flap under a Reynolds number of about 4×10^4, while at the Reynolds number of about 1.6×10^5, the propeller with a Gurney flap no longer had an efficiency advantage relative to the propeller without a Gurney flap (see Figure 29). This is also in good agreement with the optimized results by the CFD method. Thus, the CFD method has sufficient reliability for the optimization of the propeller under low Reynolds numbers.

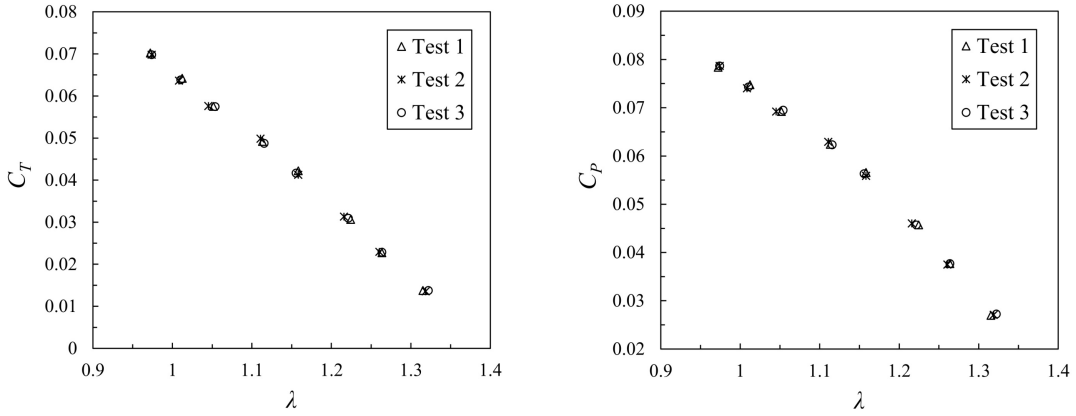

(**a**) (**b**)

Figure 27. Results of the repeated test: (**a**) Thrust coefficient vs. advance ratio; (**b**) Power coefficient vs. advance ratio.

Table 6. Comparison between two optimized propellers at the design point.

$V\infty$ (m/s)	n (rpm)	λ	$Re_{average}$	
			Prop A	Prop B
4.2	150	1.20	3.7×10^4	3.5×10^4
	178	1.01	4.2×10^4	4.0×10^4
	206	0.87	4.6×10^4	4.4×10^4
16.0	577	1.20	1.4×10^5	1.4×10^5
	685	1.01	1.6×10^5	1.5×10^5
	700	0.98	1.8×10^5	1.7×10^5

4.3. Aerodynamic Analysis

In this subsection, the aerodynamic performances of the optimized propeller with a Gurney flap (Prop B) and propeller without a Gurney flap (Prop A) are explained through aerodynamic analysis of a two-dimensional cross-sectional airfoil and a three-dimensional blade under different Reynolds numbers.

4.3.1. Aerodynamic Analysis of Cross-Sectional Airfoils

Firstly, the aerodynamic characteristics of the cross-sectional airfoils of Prop A and Prop B at a radial location of 0.75 R were analyzed. The cross-sectional airfoil of Prop A can be seen as an airfoil with 0% height Gurney flap, which was referred to as Airfoil A for convenience. The cross-sectional airfoil of Prop B is an airfoil with a 1% height Gurney flap, which was denoted by Airfoil B. In addition, their geometries are shown in Figure 30. It can be seen that the cross-sectional airfoils of A and B have similar upper and lower surface shapes except for the Gurney flap.

The aerodynamic performances of Airfoil A and Airfoil B at different Reynolds numbers (from $Re = 4.0 \times 10^4$ to $Re = 2.0 \times 10^5$) were calculated. As shown in Figure 31, Airfoil B has higher maximum lift-to-drag ratio than Airfoil A when the Re is lower than 7.0×10^4, while the situation is opposite when the Re is bigger than 1.4×10^5. As the Reynolds number increases from 7.0×10^4 to 1.4×10^5, the improvement of the maximum lift-to-drag ratio of Airfoil B relative to Airfoil A gradually decreases. When the Reynolds number reaches 1.4×10^5, the maximum lift-to-drag ratio of Airfoil B gradually changes from larger than Airfoil A to smaller than Airfoil A. To understand the reason for this change, the pressure coefficient (C_p) and streamline distributions of the two airfoils under several angles of attack near the maximum lift-to-drag ratio at four Reynolds numbers (from 4.0×10^4 to 2.0×10^5) are calculated, respectively (see Figures 32 and 33).

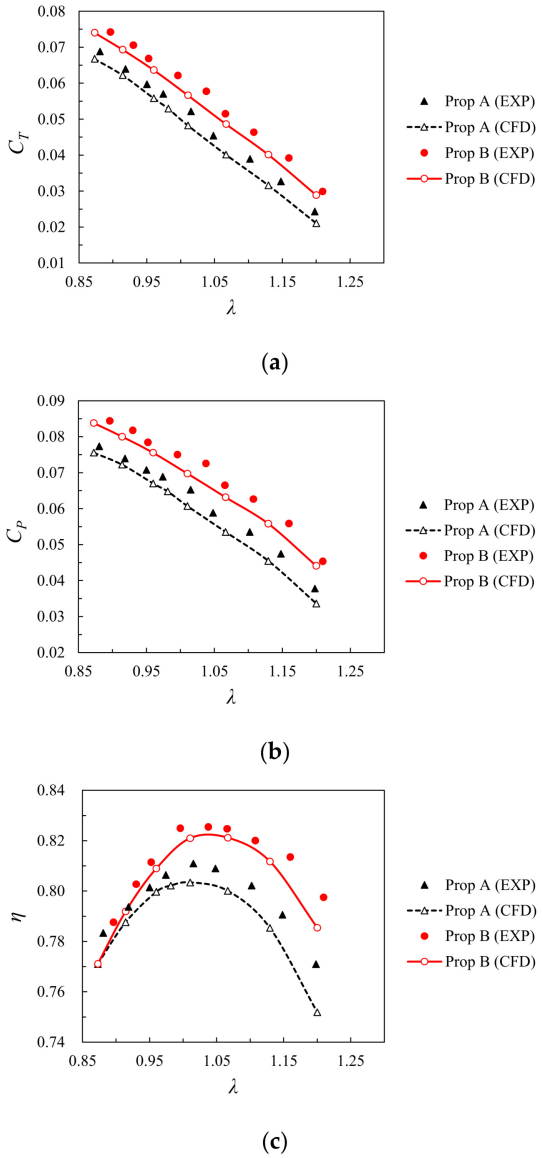

Figure 28. Comparison of the test and CFD results under $Re \approx 4 \times 10^4$: (**a**) Thrust coefficient vs. advance ratio; (**b**) Power coefficient vs. advance ratio; (**c**) Propeller efficiency vs. advance ratio.

When the Reynolds number is 4.0×10^4, the laminar separation bubbles are large and play a major role in the airfoil performance. As shown in Figure 32, since a huge laminar separation bubble markedly reduces the equivalent camber of the airfoil and increases the equivalent thickness, the lift coefficient of the airfoils is notably decreased and the drag coefficient is increased, leading to a considerable decrease in the lift-to-drag ratio. At this point, the Gurney flap helps improve this situation by increasing the equivalent camber of the airfoil. The pressure coefficient distributions in Figure 32 show that the pressure coefficient near the lower surface of Airfoil B is obviously higher than that of Airfoil A. In addition, compared with Airfoil A, the laminar separation bubble on Airfoil B can be reduced by the vortex induced by the Gurney flap. That indicates the Gurney flap could bring a significant increase in lift coefficient to Airfoil B and improve flow behavior near the upper surface. Although the Gurney flap will also bring a bigger drag coefficient to Airfoil B, the increase in lift coefficient by the Gurney flap plays a more important role to the performance of Airfoil B. This is because the lift coefficient is relatively small and the drag coefficient is relatively large at this very low Reynolds number. As a result, Airfoil B has better aerodynamic performance than Airfoil A when the α is smaller than 6° at $Re = 4.0 \times 10^4$. Besides, when α is bigger than 7°, the laminar separation bubble moves far

away from the tail edge of the airfoil and has a reduced influence on the effective camber of the airfoil. Therefore, the lift coefficient of airfoil increases significantly and becomes big enough. In this case, Gurney flap is no longer needed to supplement the lift coefficient, while it can bring additional drag. As a result, when α is bigger than 7°, the improvement by the Gurney flap diminishes.

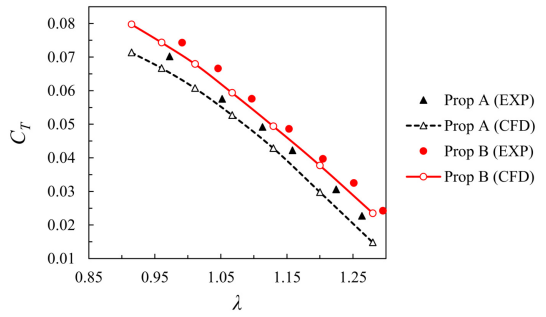

(**a**)

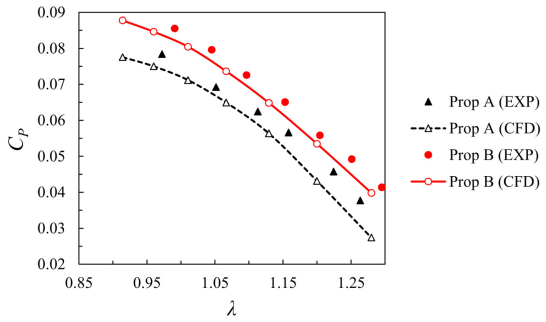

(**b**)

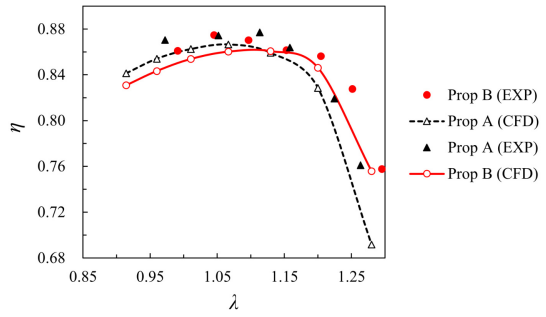

(**c**)

Figure 29. Comparison of the test and CFD results under $Re \approx 1.6 \times 10^5$: (**a**) Thrust coefficient vs. advance ratio; (**b**) Power coefficient vs. advance ratio; (**c**) Propeller efficiency vs. advance ratio.

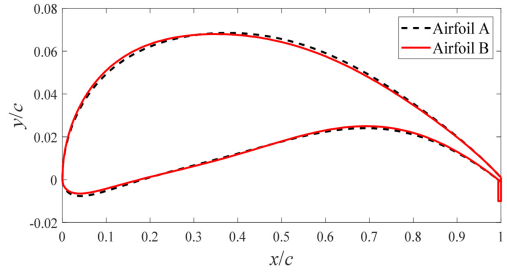

Figure 30. Geometries of the cross-sectional airfoils on Prop A and Prop B at 0.75 R.

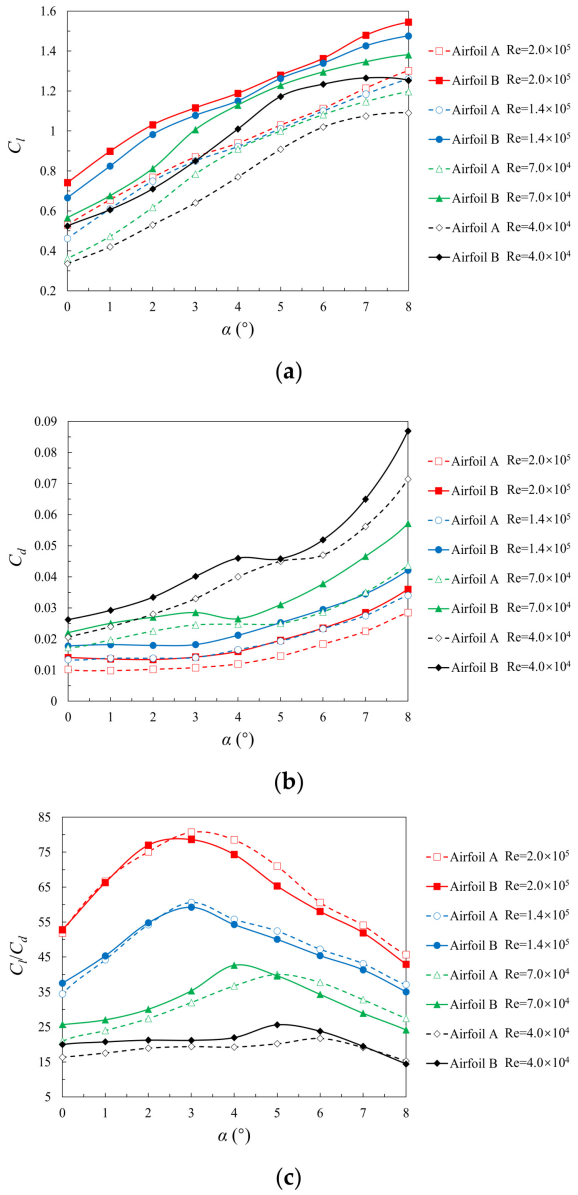

Figure 31. Aerodynamic performance of Airfoil A, and Airfoil B at different Reynolds numbers: (**a**) Lift coefficient vs. angle of attack; (**b**) Drag coefficient vs. angle of attack; (**c**) Lift-to-drag ratio vs. angle of attack.

When the Reynolds number is 2.0×10^5, the influence of inertial force on the flow increases, and the laminar separation bubbles greatly decrease and even disappear, as shown in Figure 33. It can be seen that, compared with that at $Re = 4.0 \times 10^4$, the vortices induced by the Gurney flap grow bigger, which can bring additional drag to Airfoil B. Although the Gurney flap can also bring a bigger lift coefficient, the increase in the drag coefficient by the Gurney flap plays a more important role. Because the lift coefficient of the airfoil is large enough, and the airfoil's drag coefficient is relatively small at this Reynolds number. As a result, the aerodynamic performance of Airfoil B is inferior to Airfoil A at $Re = 2.0 \times 10^5$.

Besides, it can be seen that the angle of attack corresponding to the maximum lift-to-drag ratio of Airfoil B is smaller than that of Airfoil A. That is the reason why the advance ratio corresponding to the design thrust of Prop A is smaller than that of Prop B.

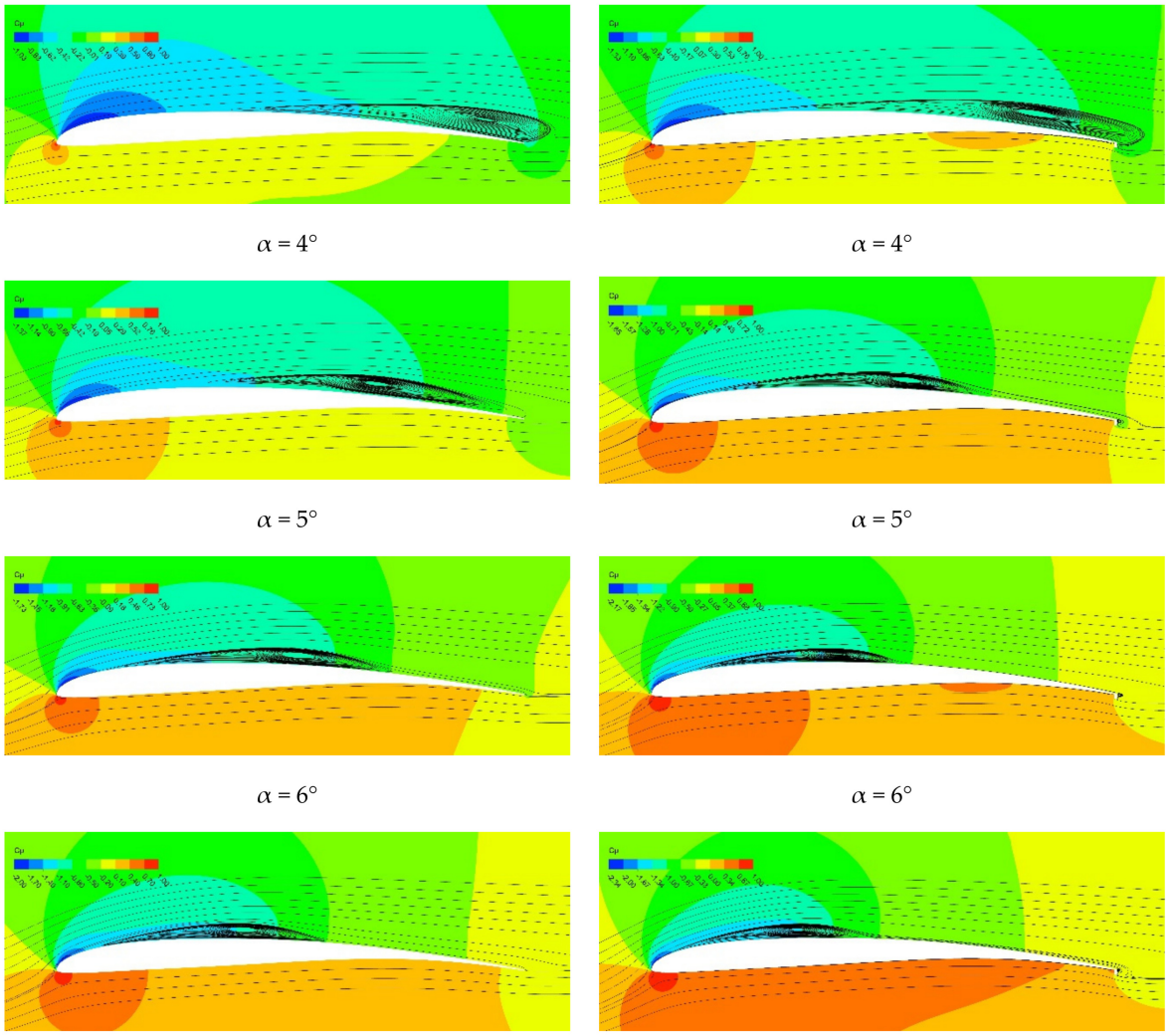

Figure 32. Pressure coefficient and streamline distributions at $Re = 4.0 \times 10^4$: (**a**) Airfoil A; (**b**) Airfoil B.

The aerodynamic analysis results of the cross-sectional airfoils preliminarily explain the reason why the aerodynamic efficiency improvement of Prop B relative to A decreased or even disappeared with the increase in Reynolds number.

4.3.2. Aerodynamic Analysis of Three-Dimensional Blades

Then, based on the analysis results of the cross-sectional airfoils, the aerodynamic analysis of the three-dimensional blades was performed to further illustrate this change of the performance of Prop A and Prop B with the Reynolds number. Two states of Prop A and Prop B were calculated by CFD method. As shown in Table 7, the design point with a Reynolds number of about 4.0×10^4 is denoted by State 1, and the state with a higher Reynolds number of about 1.8×10^5 is denoted by State 2. Figures 34 and 35 show the distributions of blade element thrust and element efficiency of Prop A and Prop B at State 1 and State 2. As shown in Figure 34, the blade element efficiency of Prop B is notably higher than that of Prop A in each station at State 1. As a result, Prop B achieved 1.8% higher efficiency than Prop A at State 1. However, Figure 35 shows that the blade element efficiencies of Prop B at most stations are slightly lower than that of Prop A at state 2. As a result, the efficiency of Prop B is 0.4% lower than that of Prop A.

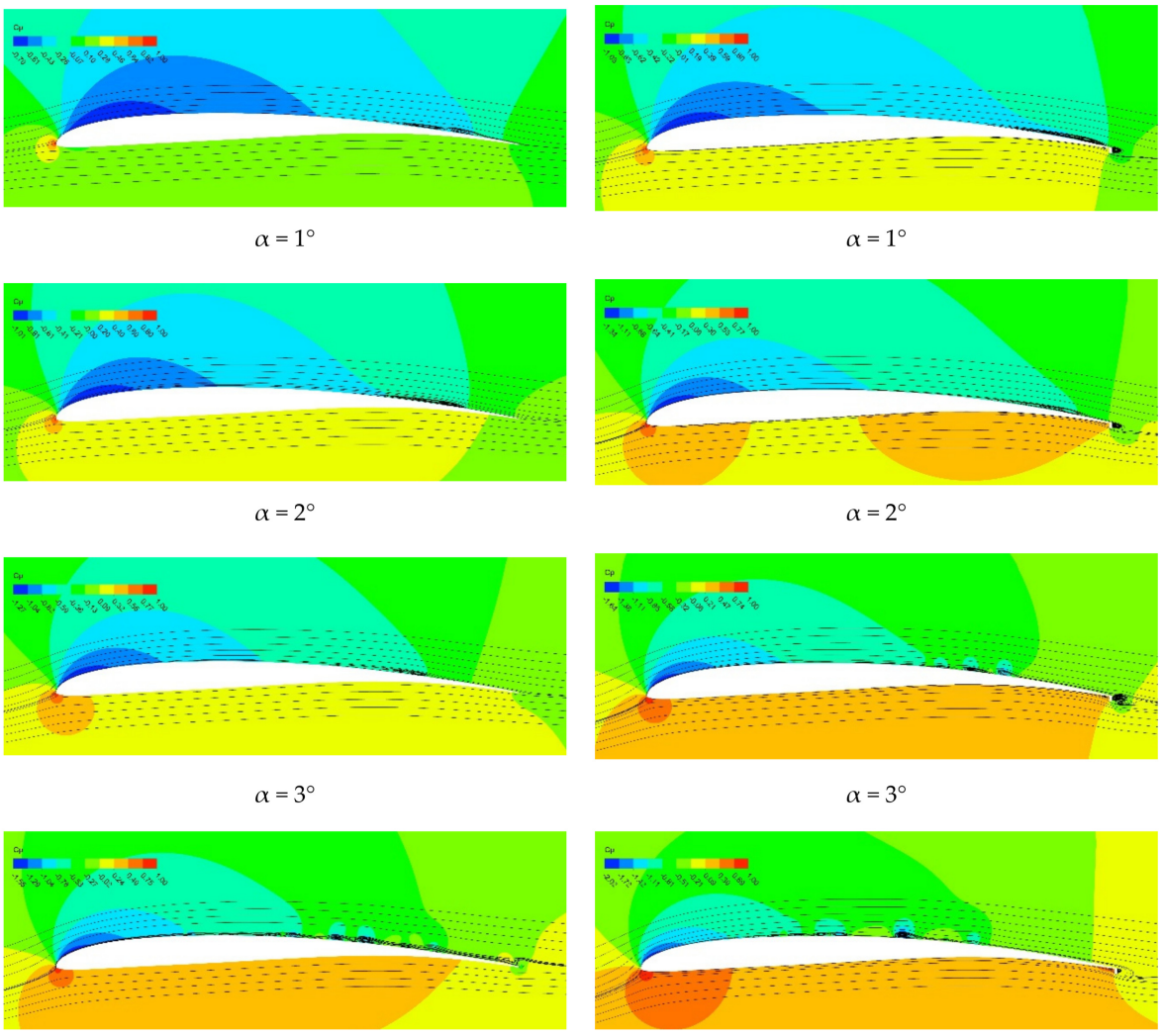

Figure 33. Pressure coefficient and streamline distributions at $Re = 2.0 \times 10^5$: (**a**) Airfoil A; (**b**) Airfoil B.

Table 7. Performances of two optimized propellers at the states with different Reynolds numbers.

Propeller	V_∞ (m/s)	State 1				State 2			
		$Re_{average}$	n (rpm)	T (N)	η	$Re_{average}$	n (rpm)	T (N)	η
Prop A	32	4.2×10^4	978	20	80.2%	1.9×10^5	978	115	86.3%
Prop B	32	4.0×10^4	948	20	82.0%	1.8×10^5	948	117	85.9%

To illustrate the reason for this change, the pressure coefficient distributions on the blades and the streamlines on the local sections ($r/R = 0.25$, $r/R = 0.5$, $r/R = 0.75$, $r/R = 0.95$) of two propellers at State 1 and State 2 are calculated, respectively (see Figures 36 and 37). Besides, the comparisons of pressure distributions between the cross-sectional airfoils with and without Gurney flaps at three radial stations of Prop B and Prop A are shown in Figures 38 and 39.

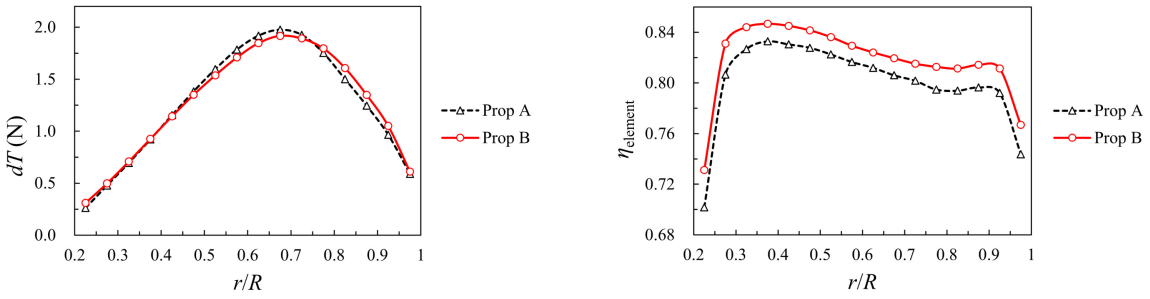

(**a**) (**b**)

Figure 34. Aerodynamic characteristics along the blade of two propellers at State 1: (**a**) Distributions of blade element thrust; (**b**) Distributions of blade element efficiency.

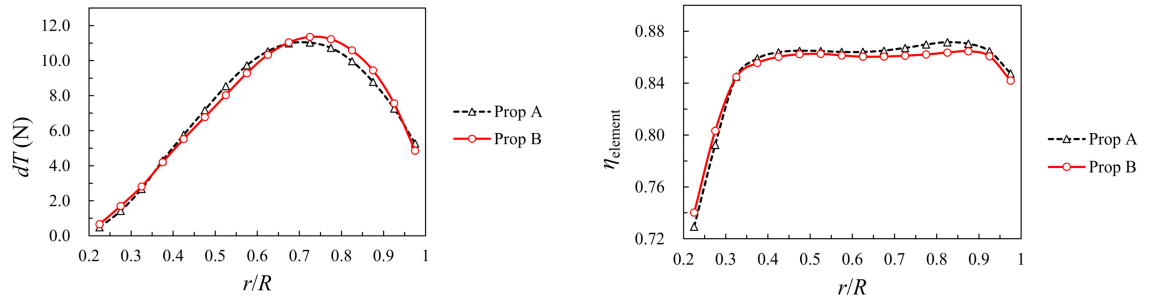

(**a**) (**b**)

Figure 35. Aerodynamic characteristics along the blade of two propellers at State 2: (**a**) Distributions of blade element thrust; (**b**) Distributions of blade element efficiency.

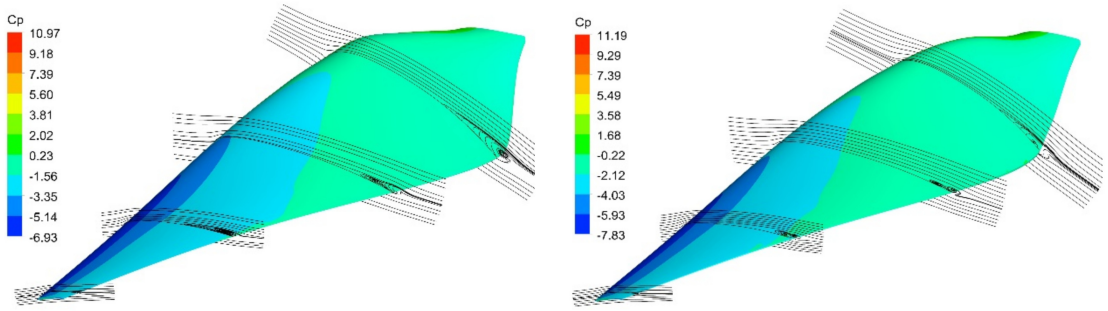

(**a**) (**b**)

Figure 36. Pressure coefficient distribution and streamlines on different cross-sections of two propellers at State 1: (**a**) Prop A; (**b**) Prop B.

As shown in Figure 36, when the $Re_{average}$ is about 4.0×10^4 (State 1), there are obvious laminar separation bubbles near the trailing edge of the propellers. Similar to the case of airfoils, the laminar separation bubbles cause a significant decrease in the efficiency of the propellers at this Reynolds number. However, in this case, the performance of Prop B can be improved by a Gurney flap. On the one hand, as shown in Figure 36, the Gurney flap inhibits the laminar separation bubbles on Prop B by the induced vortex. On the other hand, the pressure distribution results at different stations (see Figure 38) show that the Gurney flap increases the upper surface suction and the lower surface high pressure on Prop B, especially near the trailing edge, which partially offsets the lift loss caused by laminar separation bubbles. At this time, the drag caused by the Gurney flap is relatively small compared to the huge pressure drag caused by the laminar separation bubbles. As a result,

Prop B has higher efficiency than Prop A. It is worth noting that the laminar separation bubbles on the three-dimensional blades appear later than that at the cross-sectional airfoils. This is because the radial airflow caused by the rotation of the blades injects energy into the flow and delays the laminar separation.

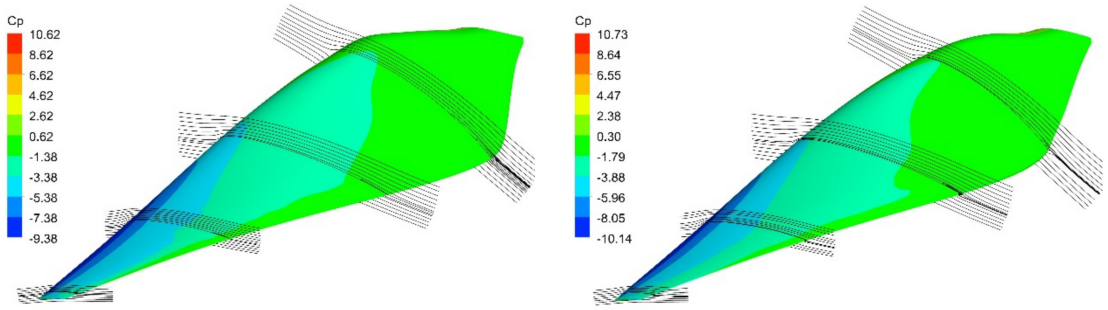

(**a**) (**b**)

Figure 37. Pressure coefficient distribution and streamlines on different cross-sections of two propellers at State 2: (**a**) Prop A; (**b**) Prop B.

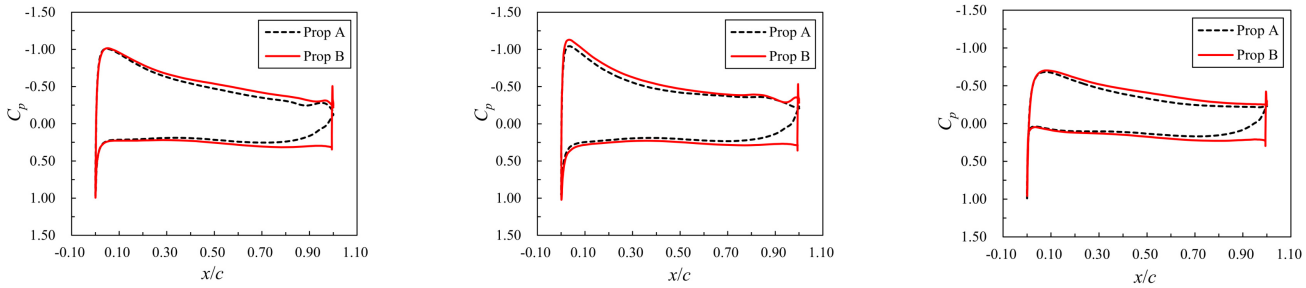

(**a**) (**b**) (**c**)

Figure 38. Pressure coefficient distribution on different cross-sectional airfoils at State 1: (**a**) r/R = 0.5; (**b**) r/R = 0.75; (**c**) r/R = 0.95.

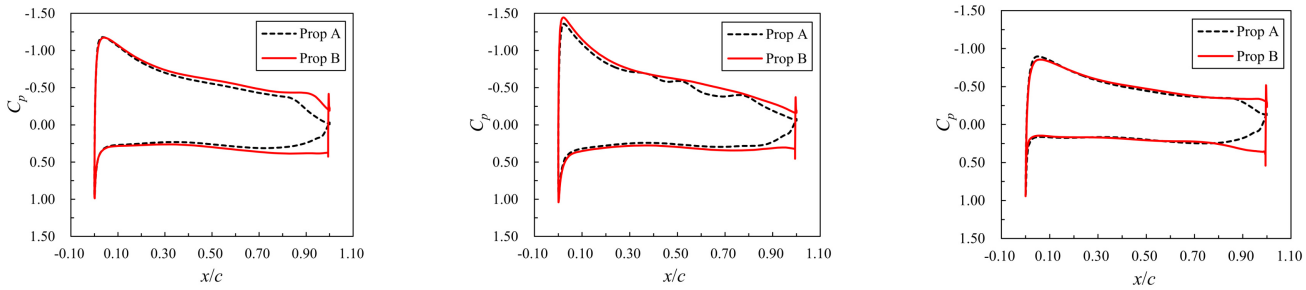

(**a**) (**b**) (**c**)

Figure 39. Pressure coefficient distribution on different cross-sectional airfoils at State 2: (**a**) r/R = 0.5; (**b**) r/R = 0.75; (**c**) r/R = 0.95.

As shown in Figure 37, when the $Re_{average}$ is about 1.8×10^5 (State 2), the laminar separation bubble almost disappears and is no longer the main factor affecting the propeller performance. As shown in Figure 39, the pressure difference between the upper and lower surfaces of the propellers at State 2 is much bigger than that at State 1, which indicates that the lift of the blade element is sufficient. In addition, since there is no laminar separation bubble, the drag of blade element is also greatly reduced. In this case, the negative effect

of the incremental drag caused by the Gurney flap outweighs the positive effect of the incremental lift brought by it. Consequently, the efficiency of Prop B is even slightly lower than that of Prop A.

In summary, a Gurney flap can affect the aerodynamic efficiency of the propeller by affecting the aerodynamic performance of the cross-sectional airfoil. The influence of a Gurney flap on the aerodynamic performance of the cross-sectional airfoil can be summarized by three factors. Firstly, Gurney flap can increase the equivalent camber of the airfoil, which can lead to higher lift coefficient to overcome the lift loss caused by laminar separation bubbles and help to improve the lift-to-drag ratio. Secondly, the vortices induced by the Gurney flap can inject energy into the airflow and help to suppress the separation bubble, which can also help improve the performance of the airfoil. Thirdly, a Gurney flap changes the pressure distribution near the trailing edge and increases the pressure drag of the airfoil. With the change of Reynolds number, the three factors account for different priorities. When the Reynolds number is as low as 4.0×10^4, due to the obvious laminar separation bubbles, the first two factors play a major role. As a result, the Gurney flap could improve propeller efficiency. When the Reynolds number increases above 1.4×10^5, the third factor plays a major role as the laminar separation bubble almost disappears. As a result, the Gurney flaps instead slightly reduces the efficiency of the propeller. Therefore, after reasonable design, the propeller with a Gurney flap can achieve better aerodynamic performance at low Reynolds numbers than the conventional propeller. However, due to the small size and high precision requirements, it is not easy to manufacture a Gurney flap on the propeller. In addition, the materials used to make the Gurney flap also require good stiffness to avoid vibration and deformation. These problems may cause difficulties to the practical application of the propeller with a Gurney flap.

5. Conclusions

In this study, an optimization method of a propeller with a Gurney flap for ultra-high-altitude unmanned aerial vehicle was established, and propellers with and without a Gurney flap were optimized under a very low Reynolds number. The aerodynamic characteristics of the optimal propeller with and without a Gurney flap were studied by numerical simulation and a wind tunnel test. Based on the results, the following conclusions are drawn:

(1) Under the same design conditions, the optimal propeller with a Gurney flap and the optimal propeller without a Gurney flap have similar distributions of chord and pitch, but the chords near the blade root of the optimal propeller with a Gurney flap are narrower and its cruising rotational velocity is slightly smaller.

(2) The advance ratio corresponding to the design thrust of the optimal propeller with a Gurney flap is smaller than that of the optimal propeller without a Gurney flap, because the angle of attack corresponding to the maximum lift-to-drag ratio of the cross-sectional airfoil with a Gurney flap is smaller than that of the cross-sectional airfoil without a Gurney flap.

(3) At the Reynolds number of about 4×10^4 (the design point), the optimal propeller with a Gurney flap can achieve 1.8% higher efficiency than the optimal propeller without a Gurney flap and reach an efficiency of 82.0% near the required thrust. Compared with the optimal propeller without a Gurney flap, adopting the optimal propeller with a Gurney flap can reduce the output power of the ultra-high-altitude unmanned aerial vehicle by 2.2%. This is because under very low Reynolds numbers, the application of a Gurney flap could significantly increase the lift coefficient of the cross-sectional airfoil at a little cost in drag by increasing the camber of the airfoil and suppressing the expansion of the laminar separation bubble. As a result, the lift-to-drag ratio of the cross-sectional airfoil with a Gurney flap increases, and the efficiency of the propeller is improved.

(4) As the Reynolds number increases, the improvement in efficiency of the propeller with a Gurney flap compared with the propeller without a Gurney flap will decrease,

and even disappear when the Reynolds number is greater than 1.4×10^5. This is because the laminar separation bubbles on the blade will decrease with the increase in Reynolds number, and its negative effect will diminish. When laminar separation bubbles almost disappear, the Gurney flap is no longer needed to increase the camber of the cross-sectional airfoil and inhibit the separation. Instead, the additional pressure drag caused by the Gurney flap would slightly reduce the lift-to-drag ratio of the airfoil, leading to a decrease in propeller efficiency.

(5) The results of the wind tunnel test show that the force coefficients and efficiencies of the optimized propellers calculated by the CFD method are in good agreement with the results of the wind tunnel test. Hence, the CFD method has sufficient accuracy, and the optimization has an evident effect.

Author Contributions: Conceptualization, Y.Y. (Yuan Yao), D.M. and L.Z.; Data curation, Y.Y. (Yuan Yao); Formal analysis, L.Z. and Y.Y. (Yayun Yu); Funding acquisition, D.M.; Investigation, Y.Y. (Yuan Yao) and Y.Y. (Yayun Yu); Methodology, Y.Y. (Yuan Yao) and L.Z.; Project administration, D.M. and L.Z.; Resources, D.M.; Software, Y.Y. (Yuan Yao) and X.Y.; Supervision, D.M. and L.Z.; Validation, Y.Y. (Yuan Yao) and X.Y.; Visualization, Y.Y. (Yuan Yao) and X.Y.; Writing—original draft, Y.Y. (Yuan Yao); Writing—review and editing, D.M. and L.Z. All authors have read and agreed to the published version of the manuscript.

Funding: This research was funded by the National Key Project GJXM92579.

Institutional Review Board Statement: Not applicable.

Informed Consent Statement: Not applicable.

Data Availability Statement: The data presented in this study are available on request from the corresponding author.

Conflicts of Interest: The authors declare no conflict of interest.

References

1. Romeo, G.; Frulla, G.; Cestino, E. Design of solar high altitude long endurance aircraft for multi payload & operations. *Aerosp. Sci. Technol.* **2006**, *10*, 541–550.
2. Joo, H.; Hwang, H.-Y. Surrogate aerodynamic model for initial sizing of solar high-altitude long-endurance UAV. *J. Aerosp. Eng.* **2017**, *30*, 4017064. [CrossRef]
3. Ma, R.; Zhong, B.; Liu, P. Optimization design study of low-Reynolds-number high-lift airfoils for the high-efficiency propeller of low-dynamic vehicles in stratosphere. *Sci. China Technol. Sci.* **2010**, *10*, 2792–2807. [CrossRef]
4. Colozza, A.J. *High Altitude Propeller Design and Analysis Overview*; NASA Glenn Research Center: Cleveland, OH, USA, 1998.
5. MacNeill, R.; Verstraete, D. Blade element momentum theory extended to model low Reynolds number propeller performance. *Aeronaut. J.* **2017**, *121*, 835–857. [CrossRef]
6. Morgado, J.; Abdollahzadeh, M.; Silvestre, M.; Silvestre, M.A.R.; Páscoa, C.J. High altitude propeller design and analysis. *Aerosp. Sci. Technol.* **2015**, *45*, 398–407. [CrossRef]
7. Adkins, C.N.; Liebeck, R.H. Design of optimum propellers. *J. Propuls. Power* **1994**, *10*, 676–682. [CrossRef]
8. Yu, P.; Peng, J.; Bai, J.; Han, X.; Song, X. Aeroacoustic and aerodynamic optimization of propeller blades. *Chin. J. Aeronaut.* **2020**, *33*, 826–839. [CrossRef]
9. Toson, U.; Hassan, A.; Owis, F.M.; Mohamed, A.S. Blade shape optimization of an aircraft propeller using space mapping surrogates. *Adv. Mech. Eng.* **2019**, *2019*, 1687814019865071.
10. BU, Y.; Song, W.; Han, Z.; Zhang, Y.; Zhang, L. Aerodynamic/aeroacoustic variable-fidelity optimization of helicopter rotor based on hierarchical Kriging model. *Chin. J. Aeronaut.* **2020**, *33*, 91–107. [CrossRef]
11. García-Gutiérrez, A.; Gonzalo, J.; Domínguez, D.; López, D.; Escapa, A. Aerodynamic optimization of propellers for High Altitude Pseudo-Satellites. *Aerosp. Sci. Technol.* **2019**, *96*, 105562. [CrossRef]
12. Qiao, Y.; Ma, D.; Li, Z. Unsteady Numerical Simulation of the Mutual Disturbance between Propeller and Wing. *Trans. Jpn. Soc. Aero. Space Sci.* **2015**, *58*, 298–306. [CrossRef]
13. Lissaman, P. Low-Reynolds-number airfoils. *Annu. Rev. Fluid Mech.* **1983**, *15*, 223–239. [CrossRef]
14. Mueller, T.J.; Batill, S.M. Experimental studies of separation on a two-dimensional airfoil at low Reynolds numbers. *AIAA J.* **1982**, *20*, 457–463. [CrossRef]
15. Ma, D.; Zhao, Y.; Qiao, Y.; Li, G. Effects of relative thickness on aerodynamic characteristics of airfoil at a low Reynolds number. *Chin. J. Aeronaut.* **2015**, *28*, 1003–1015. [CrossRef]

16. Lei, J.; Guo, F.; Huang, C. Numerical study of separation on the trailing edge of a symmetrical airfoil at a low Reynolds number. *Chin. J. Aeronaut.* **2013**, *26*, 918–925. [CrossRef]
17. Zhang, Z.; Feng, L.; Wang, J.; Liu, P. Gurney-flap drag penalty reduction with a DBD plasma actuator. *J. Aerosp. Eng.* **2017**, *30*, 4017060. [CrossRef]
18. Giguere, P.; Lemay, J.; Dumas, G. Gurney flap effects and scaling for low-speed airfoils. In Proceedings of the 13th Applied Aerodynamics Conference, Quebec City, QC, Cannada, 19–22 June 1995; p. 1881.
19. Vijgen, P.; Van Dam, C.; Holmes, B.; Howard, F. Wind-tunnel investigations of wings with serrated sharp trailing edges. In *Low Reynolds Number Aerodynamics*; Springer: Heidelberg/Berlin, Germany, 1989; pp. 295–313.
20. Traub, L.W.; Akerson, A. Airfoil Lift Augmentation at Low Reynolds Number. *J. Aircr.* **2012**, *47*, 2103–2114. [CrossRef]
21. Li, Y.; Wang, J.; Zhang, P. Effects of Gurney flaps on a NACA0012 airfoil. *Flow. Turbul. Combust.* **2002**, *68*, 27–39. [CrossRef]
22. Zhu, B.; Huang, Y.; Zhang, Y. Energy harvesting properties of a flapping wing with an adaptive Gurney flap. *Energy* **2018**, *152*, 119–128. [CrossRef]
23. Woodgate, M.A.; Pastrikakis, V.A.; Barakos, G.N. Method for Calculating Rotors with Active Gurney Flaps. *J. Aircr.* **2016**, *53*, 605–626. [CrossRef]
24. Motta, V.; Quaranta, G. Active control on helicopter blades with a L-shaped Gurney flap. In Proceedings of the 56th AIAA/ASCE/AHS/ASC Structures, Structural Dynamics, and Materials Conference, Kissimmee, FL, USA, 5–9 January 2015; p. 1854.
25. Campbell, R.L.; Lynde, M.N. Building a practical natural laminar flow design capability. In Proceedings of the 35th AIAA Applied Aerodynamics Conference, Denver, CO, USA, 5–9 June 2017; p. 3059.
26. Menter, F.R.; Langtry, R.B.; Likki, S.R.; Suzen, Y.B.; Huang, P.G.; Volker, S. A Correlation-Based Transition Model Using Local Variables-Part I: Model Formulation. *J. Turbomach.* **2006**, *128*, 413–422. [CrossRef]
27. Langtry, R.B.; Menter, F.R.; Likki, S.R.; Suzen, Y.B.; Huang, P.G.; VöLker, S. A Correlation-Based Transition Model Using Local Variables: Part II—Test Cases and Industrial Applications. *J. Turbomach.* **2006**, *128*, 423–434. [CrossRef]
28. Menter, F.R. Two-equation eddy-viscosity turbulence models for engineering applications. *AIAA J.* **1994**, *32*, 1598–1605. [CrossRef]
29. Li, G.; Wang, J. Shape Optimization of Near-Space Airships Considering the Effect of the Propeller. *J. Aerosp. Eng.* **2020**, *33*, 4020054. [CrossRef]
30. Robert, J.M.; Betty, S.W.; Betty, F.M. *Experimental Results for the Eppler 387 Airfoil at Low Reynolds Numbers in the Langley Low-Turbulence Pressure Tunnel*; NASA Langley Research Center: Washington, DC, USA, 1988.
31. Bai, P.; Li, F. *Low Reynolds Number Aerodynamics of Aircraft*, 1st ed.; China Astronautic Publishing House: Beijing, China, 2017; pp. 177–184.
32. Kulfan, B.M. Universal parametric geometry representation method. *J. Aircr.* **2008**, *45*, 142–158. [CrossRef]
33. Winarto, H. *BEMT Algorithm for the Prediction of the Performance of Arbitrary Propellers*; The Sir Lawrence Wackett Centre for Aerospace Design Technology, Royal Melbourne Institute of Technology: Melbourne, Australia, 2004.
34. Liu, X.; He, W. Performance calculation and design of stratospheric propeller. *IEEE Access* **2017**, *5*, 14358–14368. [CrossRef]
35. Wolowicz, C.H.; Brown, J., Jr.; Gilbert, W.P. *Similitude Requirements and Scaling Relationships as Applied to Model Testing*; NASA: Washington, DC, USA, 1979.
36. Jiao, J.; Song, B.; Li, Y.; Zhang, Y.; Xu, J. Development of a testing methodology for high-altitude propeller. *Aircr. Eng. Aerosp. Tec.* **2018**, *90*, 1486–1494. [CrossRef]
37. Park, D.; Lee, Y.; Cho, T.; Kim, C. Design and performance evaluation of propeller for solar-powered high-altitude long-endurance unmanned aerial vehicle. *Int. J. Aerosp. Eng.* **2018**, *2018*, 5782107. [CrossRef]